INVESTIGATION OF TRANSFER FUNCTION ANALYSIS AS A MEANS TO PREDICT STRAIN ON RAT TIBIAE FROM ANKLE TORQUE WAVEFORMS

A Thesis

by

SCOTT DANIEL BOUSE

Submitted to the Office of Graduate Studies of
Texas A&M University
in partial fulfillment of the requirements for the degree of

MASTER OF SCIENCE

December 2009

Major Subject: Mechanical Engineering

INVESTIGATION OF TRANSFER FUNCTION ANALYSIS AS A MEANS TO PREDICT STRAIN ON RAT TIBIAE FROM ANKLE TORQUE WAVEFORMS

A Thesis

by

SCOTT DANIEL BOUSE

Submitted to the Office of Graduate Studies of
Texas A&M University
in partial fulfillment of the requirements for the degree of

MASTER OF SCIENCE

Approved by:

Co-Chairs of Committee,	Harry A. Hogan
	Susan A. Bloomfield
Committee Member,	Christian J. Schwartz
Head of Department,	Dennis O'Neal

December 2009

Major Subject: Mechanical Engineering

ABSTRACT

Investigation of Transfer Function Analysis as a Means to Predict Strain on Rat Tibiae from Ankle Torque Waveforms. (December 2009)

Scott Daniel Bouse, B.S., Texas A&M University

Co-Chairs of Advisory Committee: Dr. Susan Bloomfield
Dr. Harry Hogan

Electrical Muscle Stimulation (EMS) is used as a countermeasure in animal disuse studies that seek to determine which forms of exercise are most effective in mitigating the effects of disuse atrophy on bone and muscle. Although EMS has been used for many years in our lab and others, few researchers have been able to quantify the levels of strain on rat tibiae during EMS and far fewer have investigated the causal relationship between torque produced at the ankle and strain on the tibia. This thesis sought to investigate the relationship between ankle torque and tibial strain by using a combination of techniques, namely: (1) the addition of rosette strain gages, (2) improved synchronization between ankle torque and tibial strain recordings, and (3) spectral analysis between torque and strain waveforms.

In previous work, few methods existed to align torque and strain recordings temporally, as those data were recorded on separate computers and synchronizing events were not captured. Attempting to create a torque-strain crossplot with unsynchronized data does not always yield valid results, so a method of reliably synchronizing those data is required. This thesis developed methods to capture simultaneous (synchronizing) events in both torque and strain recordings and then used those captured events to synchronize data between two computers. Following that synchronization, stiffness calculations were run on torque-strain crossplots to determine linear-model relationships between torque and strain for each method of synchronization. The results from those regressions were then used to determine if one or more synchronization techniques are superior to others, in terms of repeatability or precision. The results of these analyses

have shown that using portions of the curves can dramatically increase computing speed while providing high levels of repeatability in synchronization measures.

After synchronization techniques had been investigated, 3-element rosette data were used to calculate the principal strains on the surface of the tibiae, and the percentage of principal strains that are accounted for in the axial direction. Since the strain environment changes along the axis of the bone, the principal strain data were plotted versus the distance from proximal epiphysis to rosette gage, and statistical analysis was presented.

After rosette data were analyzed, the torque and strain data pairs were fed into a signal processing suite for the purpose of transfer function calculation. Using the synchronization methods outlined above, two means of synchronization were compared in the transfer function program. Results for these analyses demonstrated that transfer functions are slightly dependent on synchronization methods, but that calculated gains do not differ between synchronization techniques.

The specific shapes of the transfer functions highlight the relative attenuation/amplification of frequencies in torque and strain signals. Specifically, a range of frequencies, commonly called a band, between 24 and 32Hz is attenuated by the soft tissues and mechanical linkages in the lower leg of rats. This finding gives researchers looking to increase or decrease modeling stimulus to bone a new piece of information about the relative efficiency of EMS exercise. For example, EMS performed at 24-25Hz might produce less strain in the tibia than EMS at 22-23Hz, despite the 22-23Hz stimulation producing marginally less torque.

ACKNOWLEDGEMENTS

I'd like to thank my family for the 24+ years of support and encouragement I've received. Mom, I could never have made it here today without your love. Dad, I learned more from you than you'll ever likely realize, and I am grateful.

Jim, you've provided a landmark for me for years. I've found that it's easier to find your way when you can see others close to you succeeding along a similar path. I thank you, from the bottom of my heart.

I'd also like to thank the many members of the Hogan/Bloomfield lab group that supported and assisted me in this work: Jan Stallone, Liz Greene, Josh Swift, Matt Lucas, and a host of undergraduate workers.

Rosemary, you are my inspiration. I love you.

TABLE OF CONTENTS

Page

Page

LIST OF FIGURES

Page

LIST OF TABLES

Page

INTRODUCTION

Motivation

Bone serves two primary roles in the body: It serves as a calcium store for homeostatic processes, and it protects and supports bodily tissues[1]. Although calcium homeostasis is a critically important function for bone, it is not a targeted feature of bone mechanics in this thesis. However, bone's ability to structurally adapt to changes in its loading environment has a direct effect on its physical properties, and it is that ability that serves as the basal motivation behind this thesis. Changes in loading environment can come in many varieties: an individual can exercise, perform strenuous labor, take a ride into space, or sit at a desk for prolonged periods each day. Through any of these changes, the body's mechanical need for bone will change substantially.

Many studies have investigated bone's adaptation to mechanical loading, but few studies have been able to control the amount of loading on bone with a high degree of certainty. One of the more direct approaches to controlling bone loading is enforced unloading: in humans, this concept requires bed rest studies, which can be costly and time-consuming. Animal unloading studies are faster and less expensive to execute, but carry a degree of uncertainty because animals cannot be made to cooperate on the same level as a human subject could. Thus, the exercises typically applied to animal studies are less accurately controlled or recorded. This work seeks to reduce the uncertainty inherent in animal models by finding a relationship between an easily measurable metric of muscular exertion (force, torque, etc.) and a more difficultly acquired metric of bone loading (bone strain).

Previous studies by Jay Jeffrey and Brent Vyvial measured ankle torque and tibial strain in rats during electric muscle stimulation (EMS)[2,3]. While their approaches were elegant and their accomplishments notable, previous approaches have relied on data collected from multiple sources on multiple computers. There was no definitive way for past students to synchronize those data temporally, leading to an uncertainty in their

---

This thesis follows the style of the Journal of Bone & Joint Surgery.

results. Furthermore, previous work was technologically limited to strain data collected via uniaxial gages.

This study uses rosette gages and simultaneous recording techniques to not only quantify the strain environment more fully, but also temporally synchronize those data with ankle torque measurements. These results work to extend our understanding of the strain environment on bone during electric muscle stimulation.

Objectives

This study investigated the strain environment of the rodent tibia during EMS and related the measurements to both axial location and output ankle torque. Two main points were investigated: (1) Can the strain gradient be described along the axis of the tibia, and (2) Can these data be used more generally to describe the bone strains resulting from EMS in previous and future studies? These questions, expanded below, seek to identify the global applicability of strain measurements from EMS and elucidate the relationships between torque and strain on a spectral level:

1. What is the local strain environment on the surface of the tibia during EMS?
2. How does that environment change along the axis of the bone?
3. As the strain on the bone during EMS is a result of muscular contraction, can the strain be correlated with measures of muscular output (torque produced at the ankle)?
4. Can a generalized transfer function be found between ankle torque and tibial strain?
5. What kind of relationship(s) do the following parameters have on the torque-strain interaction:
    a. Location of strain measurement
    b. Orientation of a “uniaxial” strain gage

At the conclusion of the discussion outlined above, one more question may become apparent: How large would a study need to be, in terms of animals, time, and scope, to resolve the torque-strain relationship to high levels of both statistical significance and power?

BACKGROUND

Engineering Basics: Stress and Strain

In engineering, stress and strain are terms used to describe the states of loading and deflection that a material may bear. These two concepts are related by a variety of constitutive relationships, such as the elastic modulus (ratio of stress to strain) and other constants such as the Poisson's ratio (a measure of volumetric conservation).

Stress is defined as pressure, or force per unit area[4]. An example of the units of stress is the Pascal (Pa), which is listed as a Newton per square meter (N/m^2). For the remainder of this thesis, stress will serve little purpose, as the modulus of bone is not universally defined for all locations or all animals.

Unlike stress, strain can be directly measured using strain gages affixed to the surface of an object of interest. Mathematically, strain is the change in length of a sample divided by its original length, and is thus unitless. The most basic equation for finding strain is given below, and is known as simple strain.

$$\varepsilon = \frac{l - l_0}{l_0} = \frac{\Delta l}{l_0} \tag{1}$$

Simple strain is valid for small deflections[5], as long as we can safely assume that the variations in shape are small enough that changes in volume do not affect measurements of length.

One method of directly measuring surface strains is via the application of a strain gage. A simple strain gage can measure deflections in one direction only, and is commonly known as a uniaxial strain gage. Combining several uniaxial gages, each aligned to a different angle, can allow engineers to calculate strains in any direction on the surface of interest. An example of such a configuration is listed in Figure 1:

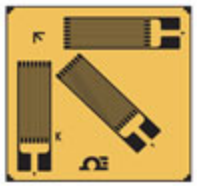

Figure 1: Example Rosette

Knowing the strains recorded from three uniaxial gages (a configuration commonly known as a rosette gage) can permit us to calculate the maximum (principal) strains, and their directions of action. The formulae to calculate strains in a specific coordinate system (aligned to the gages) are listed below[4].

$$\begin{bmatrix} \varepsilon_a \\ \varepsilon_b \\ \varepsilon_c \end{bmatrix} = \begin{bmatrix} \frac{1+\cos(2\alpha)}{2} & \frac{1-\cos(2\alpha)}{2} & \sin(2\alpha) \\ \frac{1+\cos(2\alpha+2\beta)}{2} & \frac{1-\cos(2\alpha+2\beta)}{2} & \sin(2\alpha+2\beta) \\ \frac{1+\cos(2\alpha+2\beta+2\gamma)}{2} & \frac{1-\cos(2\alpha+2\beta+2\gamma)}{2} & \sin(2\alpha+2\beta+2\gamma) \end{bmatrix} \begin{bmatrix} \varepsilon_x \\ \varepsilon_y \\ \tau_{xy} \end{bmatrix} \tag{2}$$

For 0°-45°-90° Degree rosettes, the above equation simplifies to:

$$\begin{bmatrix} \varepsilon_a \\ \varepsilon_b \\ \varepsilon_c \end{bmatrix} = \begin{bmatrix} 1 & 0 & 0 \\ 1/2 & 1/2 & 1 \\ 1/2 & 1/2 & -1 \end{bmatrix} \begin{bmatrix} \varepsilon_x \\ \varepsilon_y \\ \tau_{xy} \end{bmatrix} \tag{3}$$

This system of equations does not directly allow us to calculate principal strains, but rather it allows us to calculate the conversion to strains measured in a specific coordinate system. The equations above simplify to:

$$\varepsilon_x = \varepsilon_a; \quad \varepsilon_y = \varepsilon_c; \quad \tau_{xy} = \varepsilon_b - \frac{\varepsilon_a + \varepsilon_c}{2} \tag{4}$$

Once we have those data, we can determine principal strains using an implementation of Mohr's Circle:

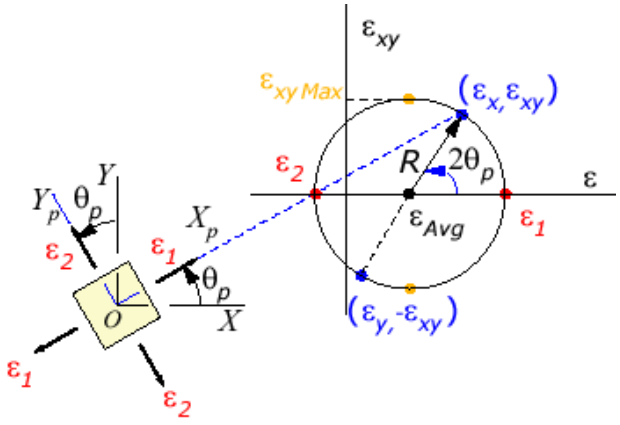

Figure 2: Mohr's Circle

From Figure 2, we can see that the maximum normal strains will exist when the shear strains have been eliminated. Based on that requirement, we can derive formulae to find principal strains ($\varepsilon_{1,2}$):

$$R = \sqrt{\Delta\varepsilon^2 + \tau_{xy}^2} = \sqrt{\left(\frac{\varepsilon_x - \varepsilon_y}{2}\right)^2 + \tau_{xy}^2}; \quad \therefore \tag{5}$$

$$\varepsilon_{1,2} = \varepsilon_{avg} \pm R = \left(\frac{\varepsilon_x + \varepsilon_y}{2}\right) \pm \sqrt{\left(\frac{\varepsilon_x - \varepsilon_y}{2}\right)^2 + \tau_{xy}^2}; \tag{6}$$

The angle the rosette makes to the direction of principal strain can be found using:

$$\theta_P = \frac{1}{2}\arctan\left(\frac{2\tau_{xy}}{\varepsilon_x - \varepsilon_y}\right) \tag{7}$$

Equations (6) and (7) will be useful later, when we begin investigating the directions of the principal strains of our *in vivo* loading system.

Classical Experiments in Bone Adaptation

In the 1970's and 1980's, several groups of researchers were investigating strain as a stimulus to bone formation. Of the many studies conducted, one of the more notable papers was an overloading study by Goodship et al.[6]. Here, the researchers removed ulnae from pigs and allowed the radii to functionally adapt for several months. They recorded bone strains from control and ostectomized groups, at time points immediately after surgery and 3 months later. From these results, Goodship found that the radii in question had adaptively modeled in the wake of an approximately 2-fold overstrain on the lone weight-bearing bone. At the conclusion of the study, the researches found that strains recorded on the adapted radii were statistically no different from contralateral controls, suggesting that the bones had 'sought' a particular level of strain, and adapted to achieve that level of loading. In their weight-matched, normally-loaded radii, Goodship found that average strains were approximately 800με. These results suggest that bone in the porcine radius is sensitive to appositional modeling influences above the 800ME level.

Another study by Qin et al.[7] showed that artificial loading on turkey ulnae promotes adaptive modeling via a non-linear relationship. A schematic of their loading regime is shown in Figure 3:

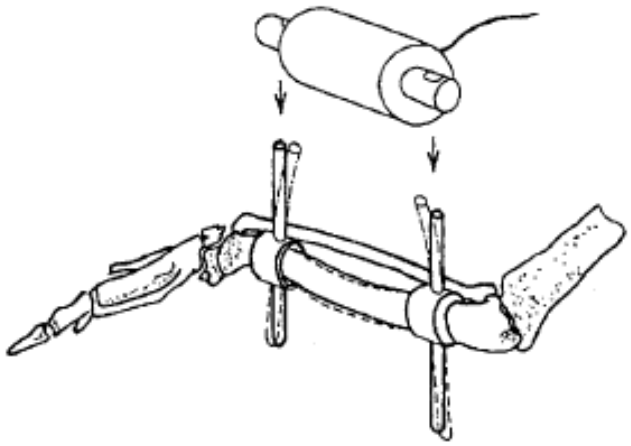

Figure 3: Schematic of Turkey Ulnae Loader (Adapted from Qin[7])

After the ulnae were isolated from loading in the wing by surgically severing both ends of the ulna and capping them off, various loading regimens were applied via pins inserted into the isolated bones. As the cycle count of low-magnitude strains increased, the researchers found bone outcomes similar to those from high-strain, low cycle count loading regimes. Their results are best shown graphically, as in Figure 4:

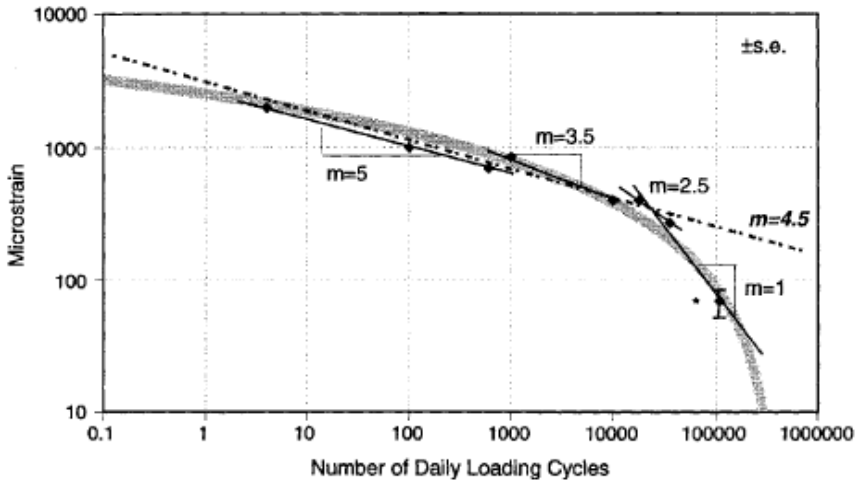

Figure 4: Qin & Rubin's Intensity-Cycle Count findings for Bone Maintenance (Adapted from Qin[7])

The studies used to produce the above graph were performed over a period of several years, and account for several loading regimes on different animal models. These researchers took results from previous work, calculated cycle counts and plotted those counts versus the loading intensity effective for maintenance of bone mass. In this way, the researchers identified a cycle count and intensity threshold for bone maintenance. Although their conclusions have been recently challenged, the quantified results they obtained are inarguable.

A parallel study by Rubin and Lanyon[8] identified strain rate as a controlling influence on adaptive modeling. In their paper, the authors provided axial compression of the ulnae via external loading, as diagrammed in Figure 5:

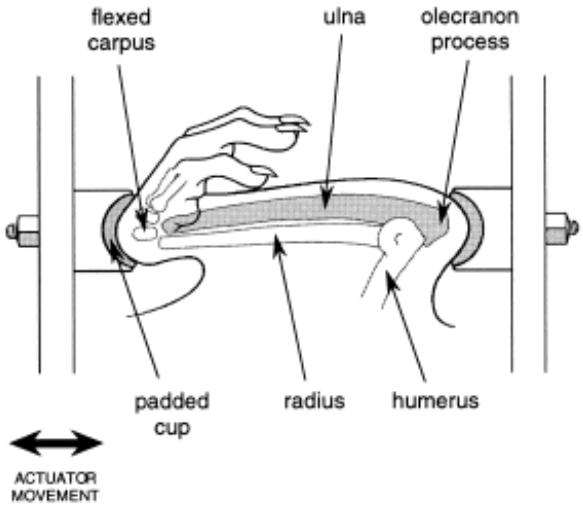

Figure 5: The Rubin – Lanyon Ulna Loader (Adapted from Rubin-Lanyon[8])

With the above diagrammed loader, the researchers were able to load the bones of interest with varying strain rates. The strain rates they had used were calculated from calibration animals at the onset of the study. Figure 6 shows their targeted strain waveforms:

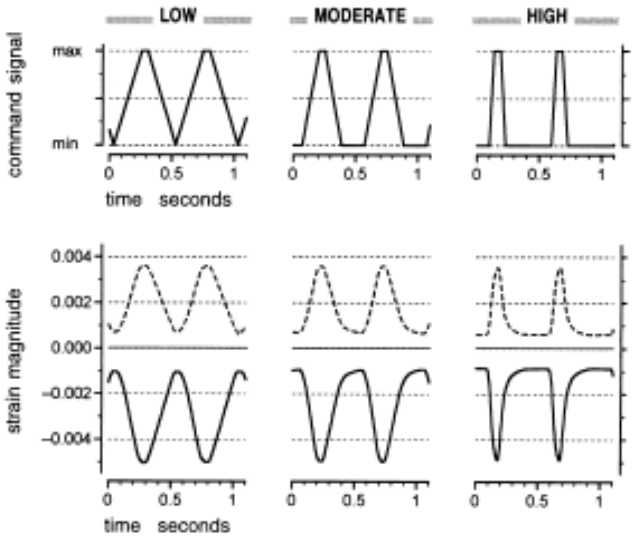

Figure 6: Rubin & Lanyon's Strain Rate Sample Groups (Adapted from Rubin-Lanyon[8])

At the conclusion of their study, Rubin and Lanyon found that strain rate and periosteal apposition rate were well correlated, even without experimental changes in strain magnitude. Hence, the most osteogenic loading paradigms were those generating higher strain rates.

More recent work has found that fluid shear stress on bone cells initiates remodeling, with work by Bacabac[9,10] showing that fluid shear stress initiates signaling pathways in osteocytes. These papers found that fluid shear stress recruits osteocytes to begin signaling for remodeling. Additionally, they also suggest that initial 'kicks' of shear stress amplify the cells' sensitivity to additional shear stress. These results are important, as we know that bone is filled with tiny channels called *canaliculi*[1]. As a bone is stressed, or subjected to strains, the fluid in the canaliculi will flow within the channels to reach pressure-driven equilibrium. As the period of the strain increases, the amount of strain required to produce a certain amount of fluid flow would be much higher than with shorter-period waveforms. This relationship should exist only to the point where the pressures oscillate so quickly that the viscosity of the fluid overcomes the driving forces, and the fluid flow is arrested. This phenomenon is called *flow choking*, and would seem to predict a plateau effect of loading frequency on modeling rate.

Whether this plateau effect actually occurs is unknown, and is outside the scope of this thesis. In contrast, some recent work on rest-inserted loading has shown that osteocytes may have a sort of latency period between effective stimuli. These papers have demonstrated that remodeling signaling is enhanced by allowing each cell to come to equilibrium before stimulating then again. In 2004, LaMothe and Zernicke[11] published an analysis of high-frequency, moderately high magnitude strains applied to mice, with and without rest inserted. Their rest-insertion paradigm is illustrated in Figure 7:

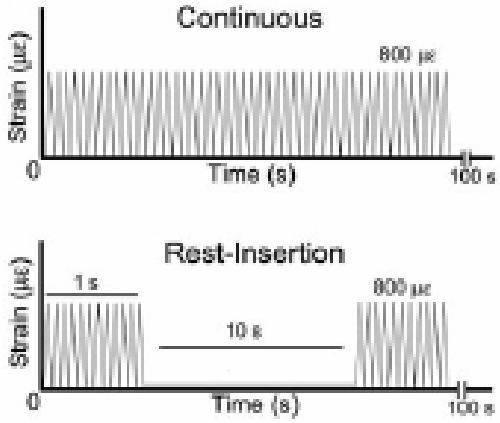

Figure 7: Lamothe's Rest Insertion Paradigm (Adapted from LaMothe[11])

Their results indicate that, in their loading paradigm, a 9.1% duty cycle for high frequency loading is sufficient to cause an osteogenic response that is at least as potent as continuous loading, if not more so. Their study relies heavily on Qin's results, discussed above, and made little mention of strain rate as a possible mechanotransduction mechanism. Additionally, this paper discusses using Fourier transforms to identify power spectra of strain waveforms. While it is not the first work to do so, their approach is worthy to note: they identified side-lobes from their loading scheme, but failed to offer that technique the scrutiny that it deserves. Specifically, those researchers saw secondary frequencies in the signal after Fourier processing and concluded that those frequencies were significant. In truth, the frequencies identified in this study did not actually exist, and instead were a result of a limitation inherent in Fourier analysis.

Other papers that investigated rest-inserted loading have been focused on mouse bones, as in Srinivasan's paper from 2007[12]. Here, the researchers found that rest

insertion at high levels of strain amplified osteogenic responses, but at an overall strain magnitude that is typically considered to be quite high (average of 1250με).

Collectively, these papers seem to indicate that periods of brief, high-rate loading interspersed with periods of brief rest would be more effective at stimulating periosteal apposition than constant loading paradigms. To this end, a recent study by Alcorn[13] has demonstrated that electrically stimulated muscle contractions can be effective at reducing or eliminating disuse osteopenia caused by Hindlimb Unloading (HU) in rats. These studies utilized EMS to load rat tibiae *in-vivo* during HU, in a set-rest exercise pattern. Four sets of five contractions each were spaced out by several minutes. In this manner, the researchers used their stimulus-rest paradigm to minimize, or even reverse, disuse osteopenia with as little as 20 minutes a day, three days a week.

Strain Gage Technology

The study on which this thesis is based used miniature strain gages to measure the strain fields on rodents' bones. Strain gages are highly sensitive instruments that change resistance when deformed. Thus, the relative deformation (strain) of a bone is measured via changes in resistance of an attached strain gage.

The circuitry that allows us to accurately measure unknown resistances is frequently called a Wheatstone bridge[14] in Figure 8, below.

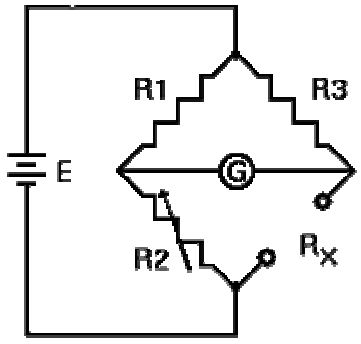

Figure 8: Wheatstone Bridge Configuration

In a Wheatstone bridge, parallel paths, of two resistors each, are connected to the same input and output signals. On one of the parallel paths, a resistor is replaced by a strain gage, whose base resistance is known. The values of the other three resistors are carefully adjusted, until the voltage between the mid-points of the parallel circuits reads zero. Then, knowing the relative values of the three known resistances allows us to calculate the value of the unknown resistor by measuring the voltage across the mid-points. The equations required to calculate these resistances are shown below:

$$V_G = \frac{R_2 E}{R_1 + R_2} - \frac{R_x E}{R_3 + R_x} \tag{8}$$

This expression can be solved for R_x, yielding:

$$R_x = \frac{E R_2 R_3 - V_g R_2 R_3 - V_g R_1 R_3}{V_g R_1 + V_g R_2 + E R_1} \tag{9}$$

Furthermore, by assuming a specialized case where $R_1=R_2=R_3$, we find that:

$$R_x = \frac{\left(E - 2V_G\right)}{\left(2V_G + E\right)} R_{1,2,3} \tag{10}$$

If we define α to be the ratio V_g/E, the resulting equation simplifies further. This new relationship is shown graphically in Figure 9, which is only valid for $[-½ < \alpha < ½]$, and has a vertical asymptote at $\alpha = -½$.

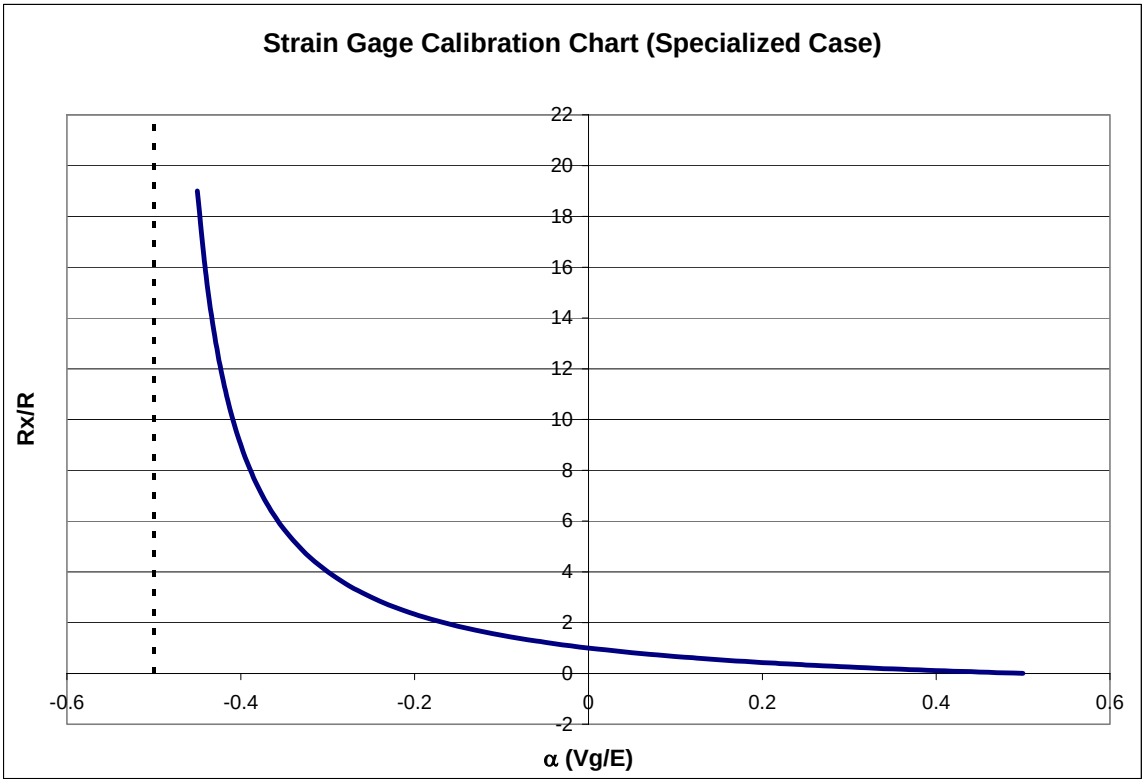

Figure 9: Sample Strain Gage Calibration Chart

Primer on Digital Signal Processing

This thesis uses analysis techniques originally derived to be used in electrical engineering to determine ex-temporal relationships between related signals. Specifically, repetitive signals that have a causal relationship between them can be related with a tool known as a Transfer Function (TF). Transfer function derivation will be covered below, but for now it may be said that a transfer function can describe the variation between two signals.

From signal theory, we know that any repeating signal can be approximated by a sum of sine waves, each at a different frequency[15]. The example below demonstrates how sine waves can be used to represent a distinctly non-sinusoidal signal. In Figure 10, we can see that the first harmonic of a square wave is simply a sine wave. As the harmonics begin to add, the sum-of-sines wave begins to approximate the square wave with ever-increasing precision.

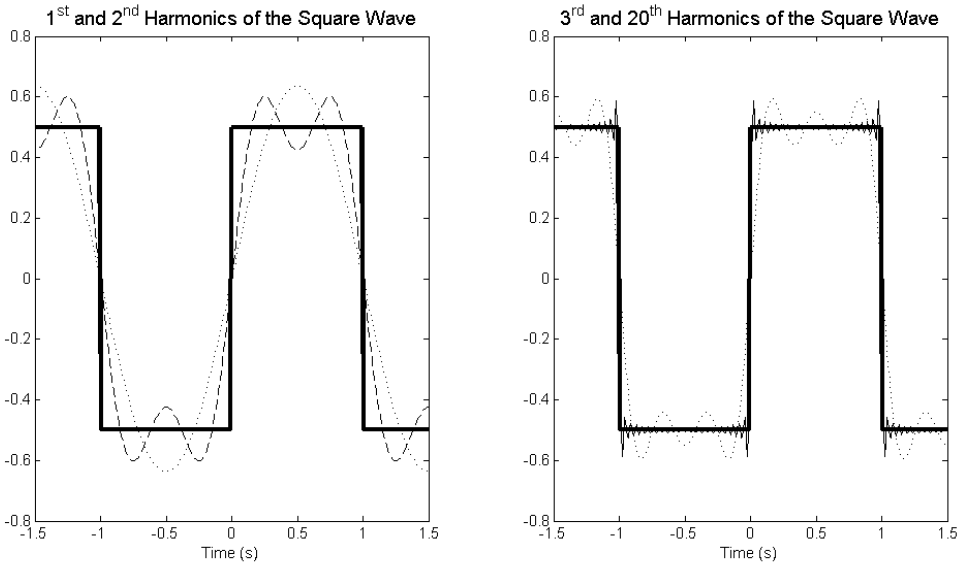

Figure 10: Sine Wave Approximation of a Square Wave

In signal processing, almost all operations are based on the Fourier Transform (FT). The Fourier transform is based on the above-mentioned theory, and uses the following equation to convert a measured signal into frequency components[16].

$$F(\omega) = \int_{-\infty}^{\infty} x(t) e^{-i\omega t} \tag{11}$$

This equation must be repeated separately for each frequency of interest, leading to a long series of numeric calculations. The Fourier transform does have limitations, which were alluded to in Figure 10. The more complex a signal, the more frequencies are needed to fully explain its fluctuations. Certain aspects of a signal, such as vertical jumps or vertical discontinuities, cannot be modeled with 100% accuracy in a continuous time system[15] because sine waves cannot have an infinite slope. This limitation is handily avoided when we sample a continuous signal for data storage and manipulation: a computer can only record discrete time points along a continuous signal, meaning it cannot ever record an infinite slope. All that is left is to convert the time-based Fourier transform formula to a sample-based transform, and run the signals of interest through the transformation. An equation showing the discrete Fourier transform is given below[16]:

$$F(\omega) = \sum_{-\infty}^{\infty} x(n) e^{-i\omega n} \tag{12}$$

The above equation, for a sample set containing N points, will require N^2 numeric calculations[17]. For large N, this number of calculations becomes extremely large, thus direct Fourier transforms are unrealistic to use. In practice, a Fast Fourier Transform[18] (FFT) can be used, whereby a sample of N points only requires $N\log_2 N$ numeric calculations. For N=1000, the FFT requires less than 1% of the calculations required by the direct Fourier transform.

Mathematically, it takes two points to describe a sine wave, meaning that 1000 samples can yield half as many frequencies, or *harmonics*[15]. The root frequency (1st harmonic) of a signal is equal to the inverse of its temporal duration, meaning that a 1-second signal can record frequencies no lower than 1Hz and a 3-second signal can record frequencies no lower than 1/3Hz. This phenomenon is purely mathematical; care should be taken to note that signals may, in actuality, represent more frequency information than can be mathematically calculated. It is also worth noting that the FFT of a signal explains the location of *every point* in the signal, meaning that all information that was captured can be represented, but there may be errors of ±9% between the points in the signal[15].

The results from an FFT are typically displayed in order of increasing frequency, meaning that for a relatively low frequency signal, the majority of the signal can be neatly approximated by the first few entries in the FFT results table. The remainder of the FFT can be thought of as completing the signal; each additional entry in the FFT corresponds to two extra points 'matched' in the original signal.

Care should be taken, here, to elucidate the difference between sampling frequency and signal frequency. In the square-wave example from above, the wave is made up of various points, equally spaced out at a specified *sampling frequency*. In contrast, the duration of the square wave determines the *signal frequency*. For example, a 10Hz signal is a data recording that captured information 10 times per second. If that capture process was continued for 2 seconds, we would have recorded 20 samples. The root *signal frequency* in the FFT would be ½Hz, and the sampling frequency would be

10Hz. Since it takes two points to describe each sine wave, we would be able to describe ten (10) sine waves, starting at ½Hz and increasing up to 5Hz.

Now that we have covered the basic rules of signal processing, we can investigate the mathematics behind transfer function calculations. Equation 12 shows that the FFT of a signal is defined as[17]:

$$F(\omega) = \sum_{-\infty}^{\infty} x(n) e^{-i\omega n}$$

The FFT can supply more information than just magnitude and phase angle of constitutive sine waves; it can quantify power levels in each frequency band. If used for this purpose, the result is known as a Power Spectral Density (PSD) plot, and represents information from one signal only. To calculate transfer functions, we require a Cross-Spectral Density (XSD) function that is capable of representing frequency contributions from two signals. The XSD function can be found by taking the cross correlation of two signals, and then the FFT of the result. Taking auto spectra and cross spectra for two signals gives us the following relations[15]:

$$S_{xx} = \int_{-\infty}^{\infty} R_{xx}(\tau) e^{-2\pi i\omega\tau} d\tau \tag{13}$$

$$S_{xy} = \int_{-\infty}^{\infty} R_{xy}(\tau) e^{-2\pi i\omega\tau} d\tau \tag{14}$$

$$S_{yy}(\omega) = \left|H(\omega)\right|^2 S_{xx}(\omega) \tag{15}$$

$$S_{xy}(\omega) = H(\omega) S_{xx}(\omega) \tag{16}$$

In the equations above, S_{xx} represents the auto-spectra, S_{xy} represents the cross-spectra, R_{xx} is the auto-correlation, and R_{xy} is the cross-correlation of the signals. Equations 15 and 16 are the primary goal of this thesis: the function H(□) is the transfer function between two signals.

In practice, this approach has several limitations: Primarily, the signals should have exactly the same number of points. Secondly, for the computed TF to be of any relevance, the signals must be sampled at the same sampling frequency, and the signals must be removed of any vertical bias (DC Offset). Once these limitations have been met,

we can investigate the results with the confidence that our approach is mathematically valid.

Advanced Signal Processing Techniques

Computing transfer functions from raw input signals can sometimes yield useful results, but more frequently, one is forced to use some advanced tools to make the signals more suitable for transfer function analysis. The tools used in this thesis are, in order of importance: digital filtering (noise removal), windowing functions (error reduction), and FFT smoothing filters.

Digital filtering is a technique used to eliminate the sometimes-potent electrical interference given off by almost all electronic equipment. Primarily, this filtering is done to remove 60Hz line-voltage noise. This noise is given off by everything plugged into the mains, and even by the wires imbedded in the walls. In this thesis' application, the 60Hz noise only appears in the strain measurements. Failing to remove the noise before computing transfer functions would result in the results being skewed artificially. It would appear as though the bones were amplifying 60Hz input energy, a condition that is fairly unlikely to occur. Digital filter design is complicated[19], and does not merit substantial discussion here; suffice to say, higher-order filters are more complicated to produce and are much more computationally intensive to execute, but yield 'cleaner' results. Figure 11 shows a typical low-pass digital filter:

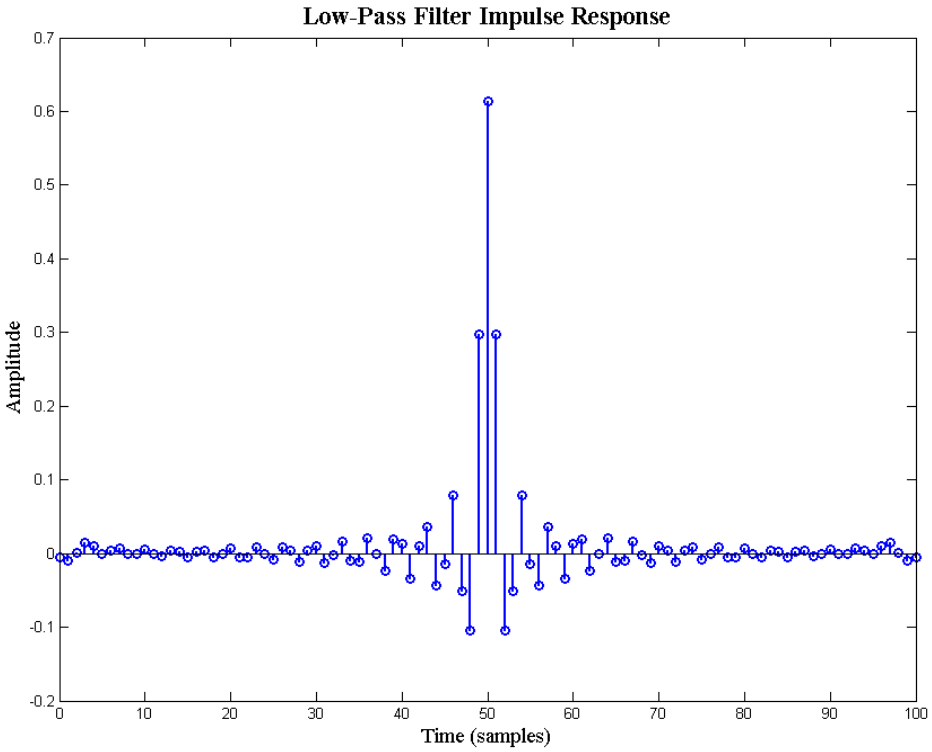

Figure 11: Typical Low Pass Filter

It should be noted, as well, that digital filters inadvertently affect amplitudes of frequencies that are not targeted. Consequently, it is advisable to filter both the input and output signals. Even though the input signals do not need filtering, the exact same phase and magnitude changes would be applied, leading to a more accurate transfer function result.

Windowing functions are signal conditioning curves designed to reduce end-to-end discontinuities in an input signal[15]. Recall that step (vertical) discontinuities in a signal require high-order frequency spectra to properly approximate them. In order to eliminate the error associated with these discontinuities, the ends of a signal are 'pinched' to zero before a FFT is processed. In this way, the beginning and end of a signal are equal (at zero) and there is no error associated with the possible discontinuity. Windowing functions have unique FFT fingerprints. Like the filtering, both input and output signals should be windowed to eliminate introduced bias[20].

There are several windowing functions available for use[15], such as Hamming, Hanning, Kaiser, Flat Top, and Kaiser-Bessel Derived (KBD). Most of these are sine-derived window functions, with the exception of Flat Top and KBD windows. The Flat Top is a Sinc waveform, and the KBD is a Bessel function-derived wide window useful for minimizing the effect of the windowing function on magnitudes of the input signals. A typical KBD window is shown in Figure 12:

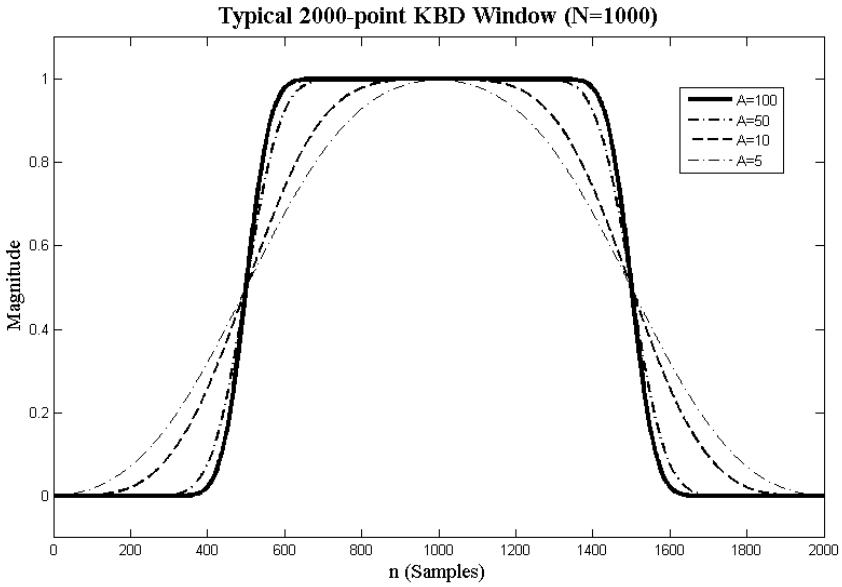

Figure 12: Typical KBD Window

Once signals are filtered, windowed, and the transfer function produced, the raw TF needs to be smoothed somewhat, before statistics can be run. Moving average filters are ideal in this case, as they smooth signals without adding much amplitude bias. Their sole purpose is to make wild fluctuations in the FFT more manageable and highlight trends within the spectra.

After smoothing, we need to average transfer functions from multiple pairs of data to eliminate subtle variations that each signal pair may contain. To get a measure of how good this averaged transfer function is, the coherence function (γ^2) value at each

frequency will be found. The equation to find coherence is given in numerous texts[15], and after simplification with Equations 15 and 16, is listed below:

$$\gamma^2(\omega) = \frac{n\left|\bar{H}(\omega)\right|^2}{\sum\left(\left|H_i(\omega)\right|^2\right)} \tag{17}$$

Equation 17, above, is the spectral equivalent to the R^2 value in time-based linear regression models. After finding coherence, the final discussion required in signal processing is a quantification of how error-free a transfer function approximation might be. As transfer functions are compiled together, their average fails to correctly approximate individual relationships. To examine the effect averaging has on spectral estimations, we turn to error estimation. A good formula for Normalized Random Error while estimating spectral content S_{xx} is[15]:

$$E = \frac{1}{\sqrt{n_d}} \tag{18}$$

In the above equation, n_d is the number of transfer functions averaged together to find the 'current' spectral estimation. For many of the results in this thesis, E will have a value of roughly .19.

METHODS

Experimental Design

Eight (8) male Sprague-Dawley rats, aged 5 months, were housed singly and fed *ad-libitum*. After acclimatization, each animal was anesthetized, and prepared for the surgical procedure. The surgical procedure, outlined in Texas A&M Animal Use Protocol (AUP) #2007-24, is given below:

After anesthetizing each animal with isoflurane, rats were removed of hair above the left tibia and femur. Betadyne surgical scrub and solution were used to prepare each animal for incision, while a sterile rosette was tested for calibration. A 2cm long incision was then made above the antero-medial aspect of the left tibia, and soft tissue gently scraped away to reveal periosteum-free bone. A drop of epinephrine was used to assist in clotting, and then the bone was dried with sterile Q-tips. After the bone was dried, the gage was removed from its sterilization packaging, and trimmed of excess backing. While this trimming procedure does affect the strain transduction properties of the gage[21], that step was necessary to ensure the gage would be properly attached to the bone surface.

After trimming, each gage was affixed to the bone approximately 12-14mm from the proximal tibial metaphysis with a drop of cyanoacrylate glue. Pressure was maintained on the rosette for 90 seconds, after which the rosette gage was firmly attached to the bone. The surface bonding was then given another 2 minutes to cure before the animal was strapped into the muscle stimulation unit. A photograph of an attached strain gage is shown in Figure 13:

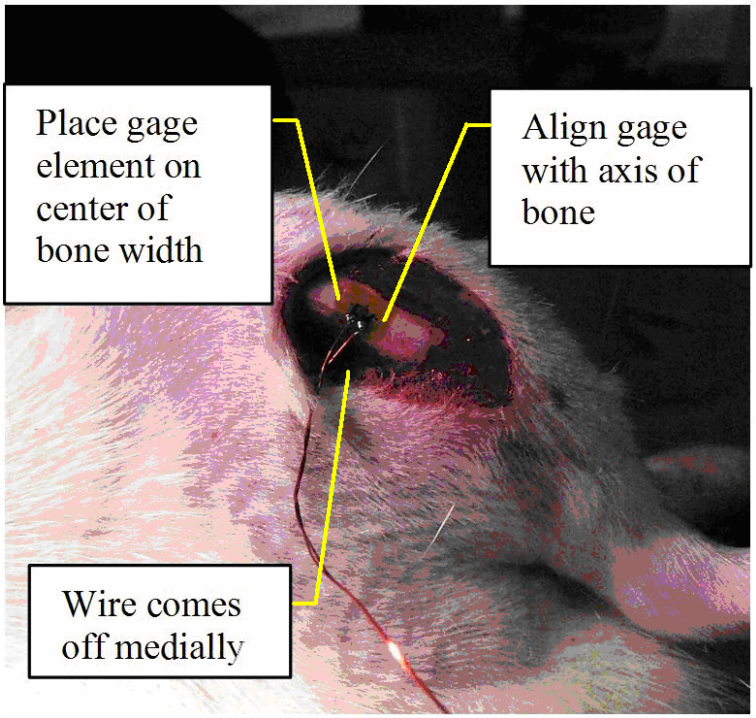

Figure 13: Proper Gage Location on Rat Tibiae

After attachment, measurements of gage location and tibial length were made, along with length of the animals' feet. Animals were then subjected to the prescribed muscle stimulation protocol. Figure 14 shows a schematic of the muscle stimulation unit[2]:

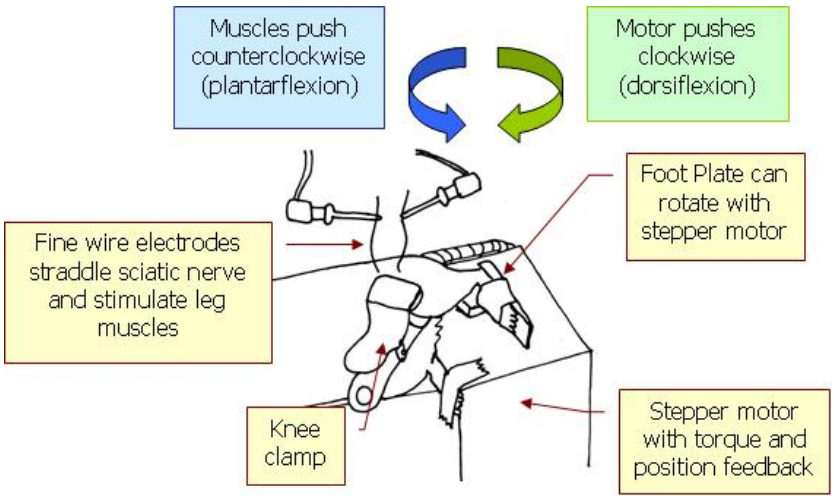

Figure 14: Diagram of the Muscle Stimulation Unit

In this study, the EMS sessions were originally done with two separate contraction groups, consisting of 400ms isometric contractions (contractions with a fixed-length muscle) and a combined isometric-eccentric contraction (contractions that incorporate a lengthening muscle during contraction). The 400ms contraction duration was chosen to provide a waveform that provided distinct and separable loading and unloading regions, while minimizing the duration of the stimulus. The analysis investigated these loading and unloading regions separately, and they will be discussed in later sections. The combined isometric-eccentric contraction typically uses 175Hz stimulation to provide tetanic contractions in the isometric phase, followed by an eccentric foot pedal sweep with concurrent stimulation at approximately 25Hz. Previous studies[1] have shown that 20Hz is a minimum stimulation frequency to cause summation of individual muscle twitches.

During muscle stimulation, data were recorded simultaneously in two computers; one computer recorded ankle torque (10kHz sampling rate for fixed-duration 1s period) while the other recorded strain measurements (5kHz sampling rate, manually controlled sampling duration). To help synchronize the data files, a novel approach was enlisted: a strain gage was affixed to the foot pedal of the muscle stimulation system. In this way, we were able to indirectly record the reaction forces on the foot pedal (by the resulting strains), and match the waveforms measured in the strain computer with the torque

waveforms taken by the torque machine. Figure 15 shows the location of the strain gage on the muscle stimulation foot pedal:

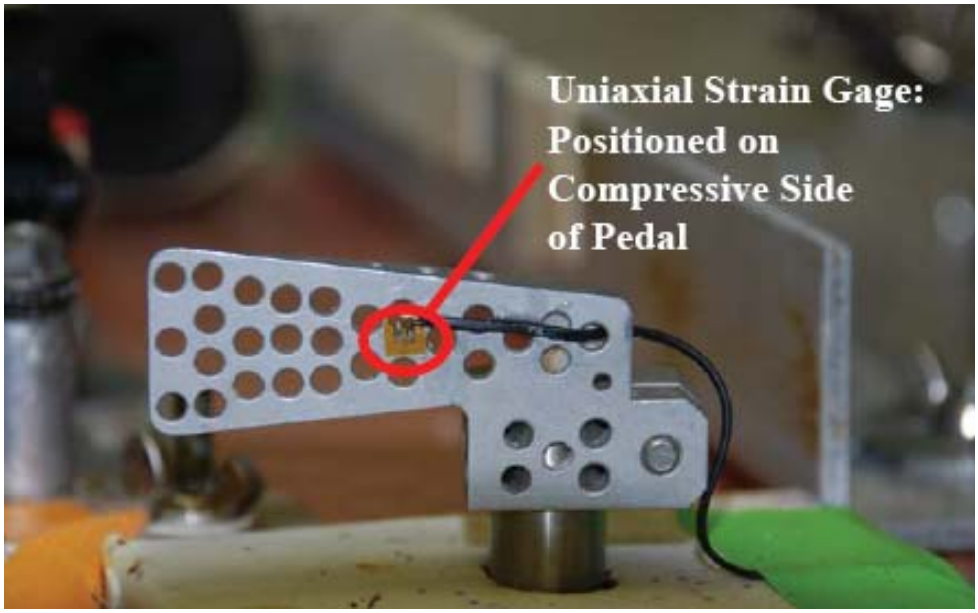

Figure 15: Strain Gage Location on the Muscle Stimulation Unit

Data Synchronization Methods

After data were recorded, strain data were reduced to ASCII text files, and both torque and strain data were transported to the computer lab for analysis. Custom-written MATLAB (The MathWorks, 2008) M-files were employed (Appendix A) to: (1) find peak-to-peak strains for the tibiae, (2) make corrections for principal strain directions, (3) find synchronization values from each data file pair and visualize the parametric Torque-Strain plots.

To find synchronization data for each point-pair, strain from the foot pedal was rectified and filtered to remove 60hz noise. After removing the DC offset of the strain trace, pedal strain was normalized by peak strain, to produce a signal of unit amplitude. The same technique was applied to the torque recordings so that the signals could be compared with maximum certainty, but with one additional operation: since the torque data were recorded at twice the sampling rate, they had to be decimated (resampled) to match the sampling frequency of the strain recordings. The traces were then shifted in

time with respect to one another, and the sum of the differences between the signals was computed. The formulae to accomplish this sliding summation are listed below, where $L_{\square}$ and $L_{\square}$ represent the lengths of torque and strain recordings, respectively:

$$D(i) = \sum_{j=0}^{L_\tau} \left| \varepsilon(i+j) - \tau(j) \right|; \quad 0 \le i \le (L_\varepsilon - L_\tau) \tag{19}$$

Once this sliding summation had been accomplished, the function D could be analyzed for local and absolute minima. The absolute minimum value of D represents the maximum agreement of the torque and pedal strain recordings. Figure 16, below, shows a typical "D" curve:

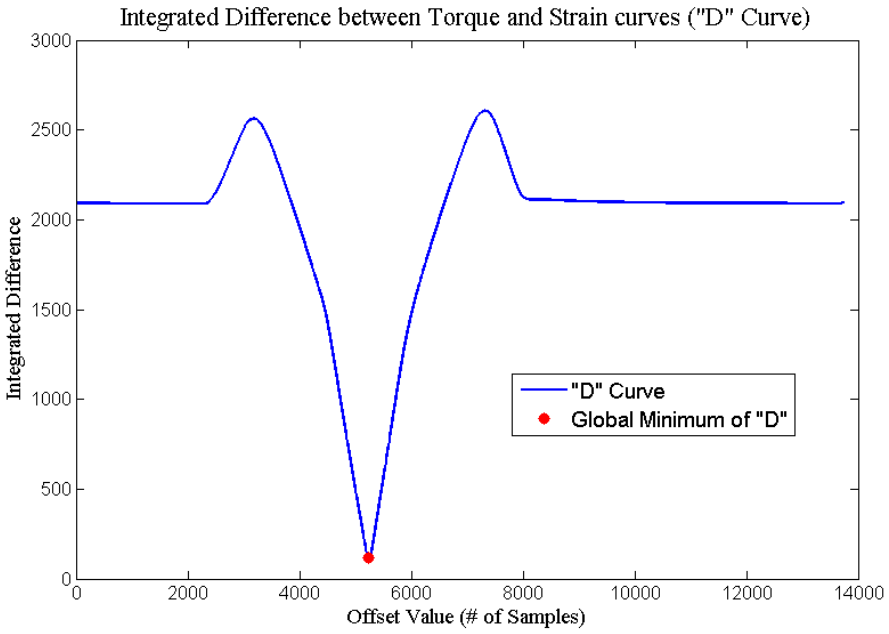

Figure 16: Typical "D" Curve

From these data, the minimum of D was found. The location in D of the minimum represents the offset, or time-shift, between the torque and pedal strains. After locating the minimum, the index value of the minimum of D was recorded in a spreadsheet for later analysis.

At this point, it is worth noting that mathematical minimization of whole-signal differences is not the only means to synchronize data. By isolating various components of the torque curve, we can match rising slopes, falling slopes, curve 'toes,' or any other identifiable features that both signals share. The axial strain trace was then synchronized using the above-described methods, for contrast. These alternative analyses were computed, and results are listed in greater detail in the results section below. Additionally, after finding the minima of D, the offset values could be used in creating parametric torque-strain curves.

Rosette Data Analysis

While our strain recording capacity was limited to three channels, we were able to collect 'full' rosette data by sacrificing data collection on the foot pedal for a small percentage of strain recordings. As mentioned previously, finding the directions and magnitudes of principal strains requires three single-element rosettes aligned in a known geometry. From Equations 6 and 7, we can determine the magnitude and orientation of peak strains on the tibiae. In practice, the strain data tends to 'float' away from zero during a muscle stimulation session, so data needed to be post-processed to determine principal strain data from the reduced strain data. The procedure for post-processing is listed below, with a full flowchart listed in Appendix A:

1. From the raw strain data, the muscle stimulation event is identified.
2. For each of the three strain traces, the stimulation event is filtered and zeroed in a custom-written MATLAB program (DATMeT, Scott Bouse) designed to maintain temporal relationships between many input signals.
3. For the newly processed data, principal strain magnitude and angles were calculated, and the results plotted alongside the axial strain trace.
4. Angle traces were then analyzed for strain angle at peak principal strain.
5. Those results were reported to a spreadsheet, and are summarized in Results.

Spectral Analysis

For spectral analysis, data were imported into DADiSP (DSP Development Corporation, 2002), a signal processing suite with advanced capabilities. This step was taken to ensure that coding errors could not introduce inconsistencies into the spectral data. The full pseudo-code for spectral analysis is listed in Appendix A, but a short list of the actions taken is given below:

1. Import Data
2. Filter, Demean Data
3. Compute Transfer Functions
    a. Report to spreadsheet
4. Calculate average Transfer Function
    a. Report to spreadsheet
    b. Normalize by High-Frequency Average
5. Compute Coherence Functions
    a. Report to spreadsheet

It is worthy to note that the delay function $\delta(t-t_o)$ has a spectral equivalent equal to the complex exponential waveform (e^{-jwt}). In other words, spectral analysis does not fully escape the need for data synchronization. Figure 17 shows the delta function in both time and frequency space:

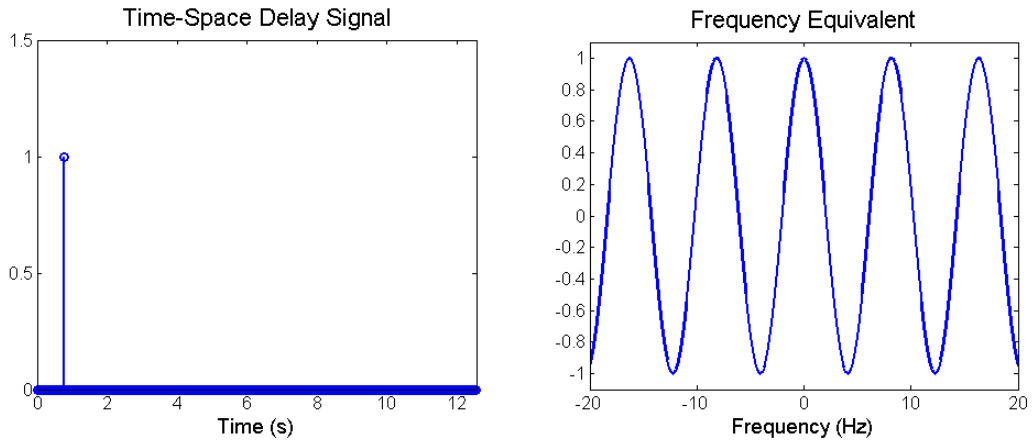

Figure 17: Time and Frequency Equivalent Signals

To address the need for data synchronization, we used the synchronization values previously tabulated to minimize the effect of mathematical delay. After applying appropriate data conditioning steps, we outputted the data to spreadsheet for further analysis.

Statistics

The statistics used in this thesis are based on the Analysis of Variance (ANOVA) algorithm, the student t-test (T-test), and linear regression statistics. Specifically, measures of signal amplification and delay calculations will be weighed for significance using pairwise t-tests, while parametric plots use linear regression methods to acquire linearized relationships between input and output. A good reference for those algorithms is *Applied Statistics for Engineers and Scientists*[22].

RESULTS / DISCUSSION

Synchronization

After the strain data were collected, synchronizing the torque and strain data became the next step in the analysis. Figure 18, below, shows the results of a typical set of synchronization curves, and the resulting offset values that they produce.

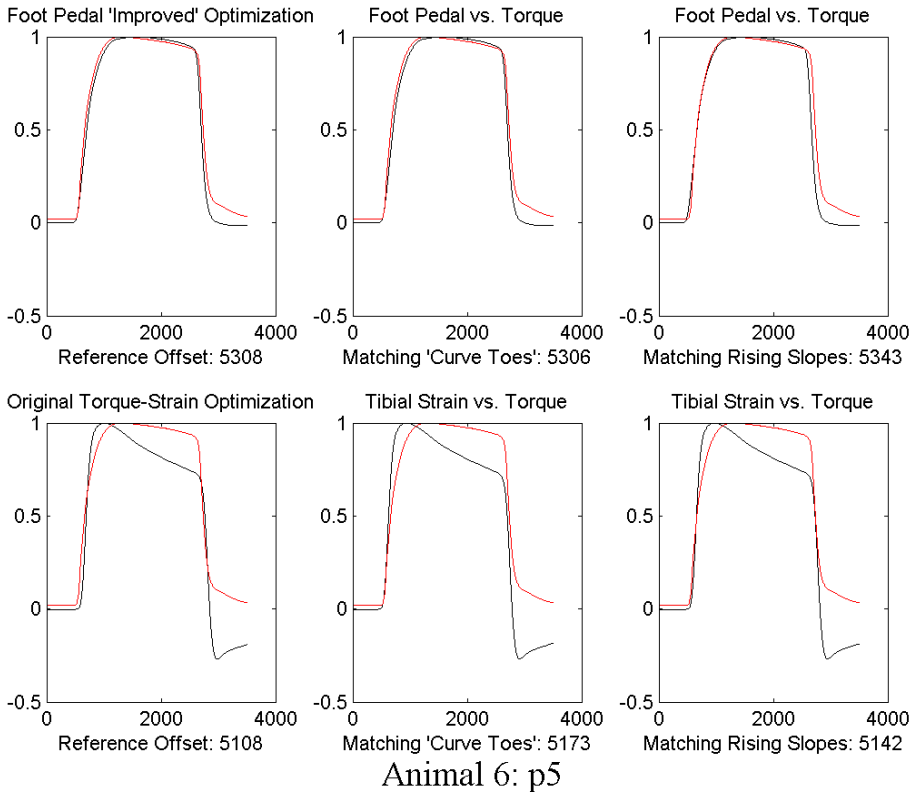

Figure 18: Effects of Different Synchronization Subroutines on the Alignment of Torque and Strain Curves. The ordinates of these graphs are in samples, and the abscissas are in normalized amplitude. The top row demonstrates variations on foot pedal strain synchronization, while the bottom row demonstrates variations on tibial strain synchronization

The global results of the above procedures are outlined in Table I, below:

Table I. Results of Synchronization Routines

Delay Values compared to The Pedal Strain Total Signal Optimization (baseline)	Samples ±SE	Seconds (±SE)
Pedal Strain Toe	3.96± .28	0.001±(5.5E-5)
Pedal Strain Rising Slope	-32.58± .28	-0.01±(5.5E-5)
Tibial Strain Total Signal Optimization (Jeffrey 2006)	158.71± 1.21	0.03±(2.4E-4)
Tibial Strain Toe	127.65 ± 2.59	0.03±(5.2E-4)
Tibial Strain Rising Edge	108.54± 1.80	0.02±(3.6E-4)

*The Samples column is a count of the amount of time (in sample count) that the synchronization routine altered the relationship between input and output signals. Seconds represents the number of seconds corresponding to 1/5000 of Samples.

Linear regressions between pedal strain toe synchronization and tibial strain toe synchronization show that tibial strain values lead (precede) torque values by approximately 0.025s. These results indicate that a standardized delay may be used to concretely determine torque vs. strain offset delays. Moreover, these data suggest that strain in the tibia occurs before torque production at the ankle. This result can be logically justified because a muscular contraction must act on bone before it can produce motion. Complete results of all statistical analyses are shown in Appendix B.

Based on the offset values calculated in the previous paragraphs, we can produce parametric torque-strain plots, similar to those produced by Jeffrey (2006). Figure 19 shows the same torque and strain data as above, but at different synchronization values:

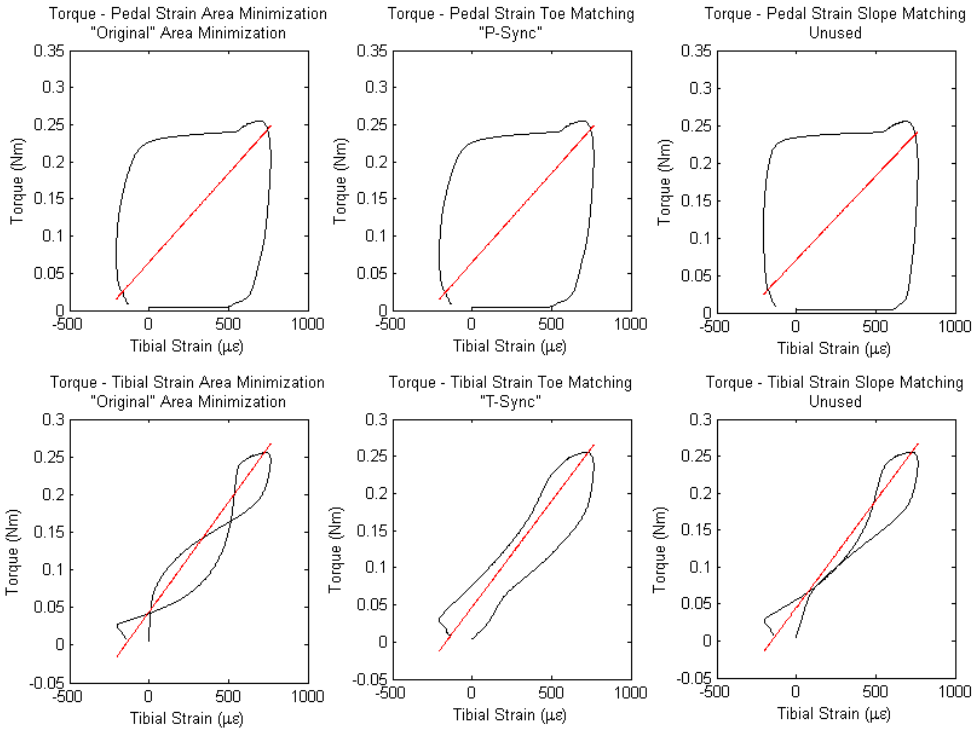

Animal 6: Parametric Plots of Torque vs. Strain for Varying Synchronization Routines

Figure 19: Parametric Plots of Torque vs. Strain for Different Synchronization Values

The figure above demonstrates how crucial proper synchronization is to analyzing parametric plots of torque and strain. Small differences in synchronization can alter linear-model calibration parameters substantially. Table II shows the average differences in linear regression calibration parameters due to choice of synchronization routine:

Table II. Linear-Model Calibration Coefficients for Various Synchronization Protocols

Strain Trace Used	Synchronization Method Used	Average Stiffness by Linear Regression (με/Nm) ± SE	Average R^2 of Regression
Pedal Strain	Whole Curve Matching	2408.7 ± 240.9 $^{\mu\varepsilon}/_{Nm}$	0.71
	Curve Toe Matching	2378.3 ± 239.3 $^{\mu\varepsilon}/_{Nm}$	0.73
	Rising Slope Matching	2548.8 ± 254.3 $^{\mu\varepsilon}/_{Nm}$	0.64
Tibial Strain	Whole Curve Matching	2048.8 ± 202.3 $^{\mu\varepsilon}/_{Nm}$	0.93
	Curve Toe Matching	2087.0 ± 203.5 $^{\mu\varepsilon}/_{Nm}$	0.90
	Rising Slope Matching	2066.9 ± 202.1 $^{\mu\varepsilon}/_{Nm}$	0.92

In Table II, we see that the stiffness values are generally higher in the P-sync curves than in the T-sync curves, but with a detriment to regression R-values. This shift corresponds to higher levels of strain at the initial phases of torque production (strain leads torque in time). The differences will be accounted for in later sections of this text.

Discussion of Synchronization Results

The synchronization values, listed in Table II, found by matching whole torque and whole pedal strain signals were not substantially significantly different from those found matching the toe curves. This result allows the (faster) curve toe synchronization to be used in place of the more mathematically-rigorous full-signal synchronization.

After inspecting the parametric torque-strain curves produced by the various synchronization routines (Appendix C), it becomes clear that the tibial strain curve toe is the more repeatable method of the three to synchronize those data with Torque recordings. Subjectively, the parametric curves produced by the T-Sync algorithm cross with much less frequency than either the area minimization or the rising edge algorithms. Since these data are the most repeatable of the three methods used, they were chosen for use in the remainder of the study. It is a happy coincidence, then, that the preferred methods of synchronization were toe matching for both the Pedal strain and Tibial strain traces, and it lends an appreciable level of symmetry to this study. For the remainder of this thesis, comparisons will be run between synchronizations based on the toes of either the tibial strain (T-Sync) or the pedal strain (P-Sync).

These results bring up an interesting point: an experimenter must be careful not to create results via his/her analysis system. Certain synchronizations produce more variability in linear parameters than others, and can alter statistics calculations as well. This limitation is a primary reason why this thesis is focused more on transfer function analysis than on parametric plots.

Results of Rosette Strain Analysis

One of the most basic, but intriguing, findings from this thesis has been that recorded strains on the metaphyses of rat tibiae are tensile during muscle stimulation. The majority of strain recordings taken for this thesis show tensile strain recordings. This observation is backed by binomial probability distribution (Appendix B).

The primary reason for enduring the additional cost and complication of using rosette gages on rat tibiae was to determine principal strains and principal directions. Following that prompt, the value of maximum principal strain was calculated for each animal that received a rosette gage, then the axial measurements were normalized by their corresponding maximum principal strains. These results are best shown in Figure 20:

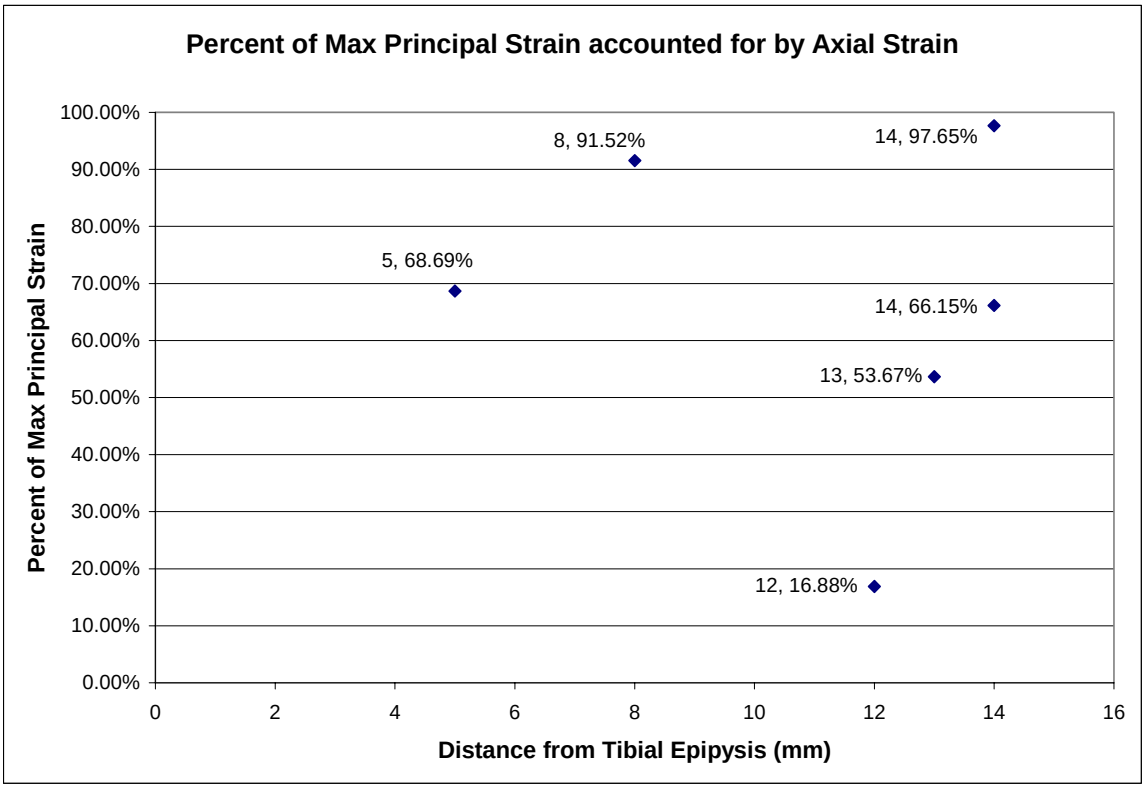

Figure 20: Percent of Max Principal Strain Accounted for by Axial Strain

These data do not fit a linear trend. Variations in gage placement across the width of the antero-medial aspect are likely to blame for these results. Unfortunately, these bones were not preserved, so there is no way to determine whether cross-axial location had a substantial impact on the gage readings shown above.

In order to accurately measure the results from this thesis against that of previous work, I present an illustration of peak torque to peak strain ratios. These correlations were also performed in theses by both Vyvial and Jeffrey and are mirrored here for reference by interested readers (Figure 21). The main difference between the preceding work and this thesis' results is that principal strains were chosen to represent strain values instead of axial strains. There are variations in these results, which are likely due to differences in surgical technique or individual preference in gage placement.

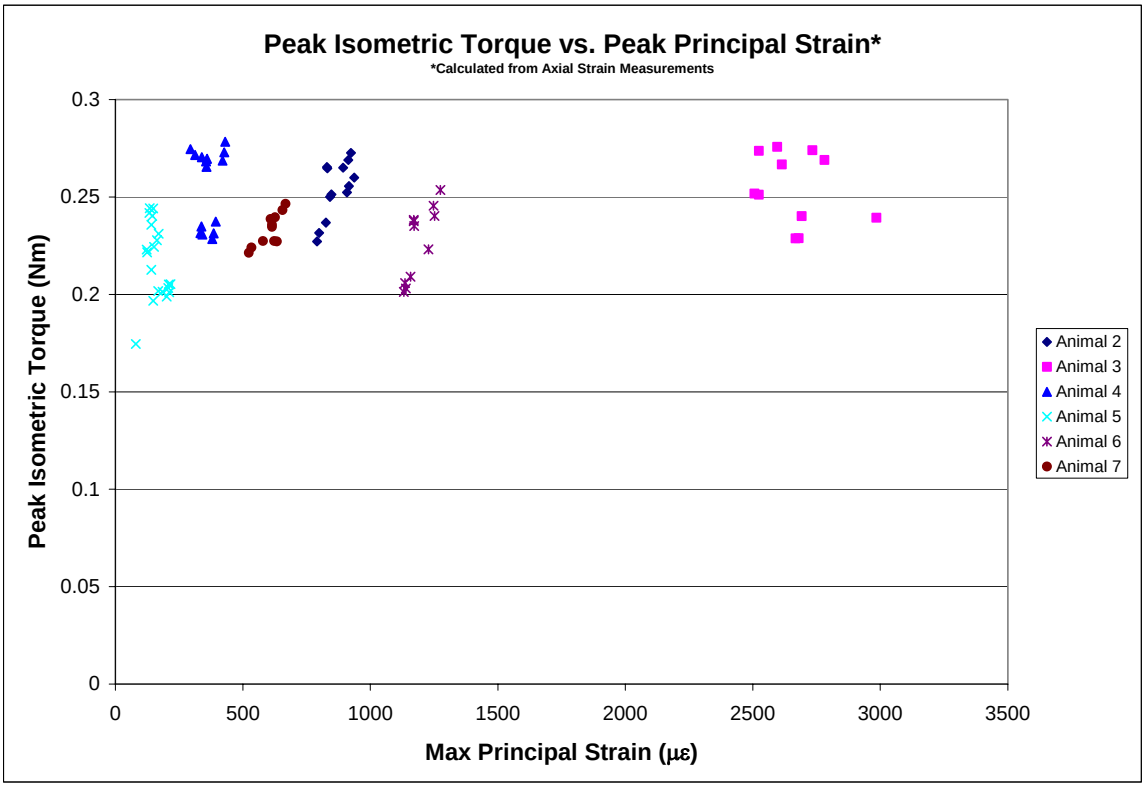

Figure 21: Peak Strain and Peak Torque for Each Animal's 6-12 Data Points

These data have a highly variable maximum principal strain, but similar torque levels, meaning they do not suggest a universal linear correlation between peak strain and peak torque.

Discussion of Rosette Strain Analysis

The dissonance of the principal strain data in Figure 20 is disheartening. Initially, one would expect that the more advanced technology used would allow us to capture a broader picture of unknown phenomena. The original intent was that by calculating principal strains, one could eliminate gage orientation errors. Then, the principal strains would allow a truer correlation between strain and torque. Unfortunately, this expectation is not reality: The results simply do mot support the intentions of this section of the study.

This author proposes a thought as to why the rosette data (Figure 20) are so incongruent. The tibia is curved along its axis and all muscle groups act on the opposite side of the tibia from the gage location[23]. From that knowledge, it is easy to understand how a complex relationship between exact gage location and principal strain magnitude could exist. Based on that understanding, one might expect to see highly varying strains along the width of the tibial metaphysis: The most tensile strains would be expected opposite the combined lines of force for the contracting muscles, while the neutral bending axis would theoretically exist in zero axial strain. Since the metaphysis of the rat tibia is typically less than 5mm wide, the gage elements used span 16% of the total width. The prewired pads accounted for a much larger portion of the total tibia width, and were commonly positioned below the gage elements on the bone. This means that most measurements with rosettes were from a point closer to the anterior edge of the tibia than previous measurement techniques. Experimental or procedural error could also account for a portion of these findings. Specifically, an error in placement of half a gage-width would account for about 8-10% of the tibia's total width Unfortunately, these tibiae were not saved, so post-procedure evaluation is not possible.

Another possible candidate for these differences is a difference in the adhesion between bone and gage. Although great care was taken to ensure that the gages were properly affixed, experimental error is impossible to rule out.

Transfer Function Analysis Results

After finding that curve toe synchronization is the most repeatable method of the methods investigated, data files were fed into a DADiSP macro for further processing. Simultaneously, transfer functions were computed for both T-Sync and P-Sync offset values. Recall that transfer functions relate frequencies in an 'input' signal to those in an 'output' signal. The curve is a function of frequency, and the amplitude is the ratio of strain to torque in that frequency range. Figure 22 shows a typical 80-Hz representation of a transfer function:

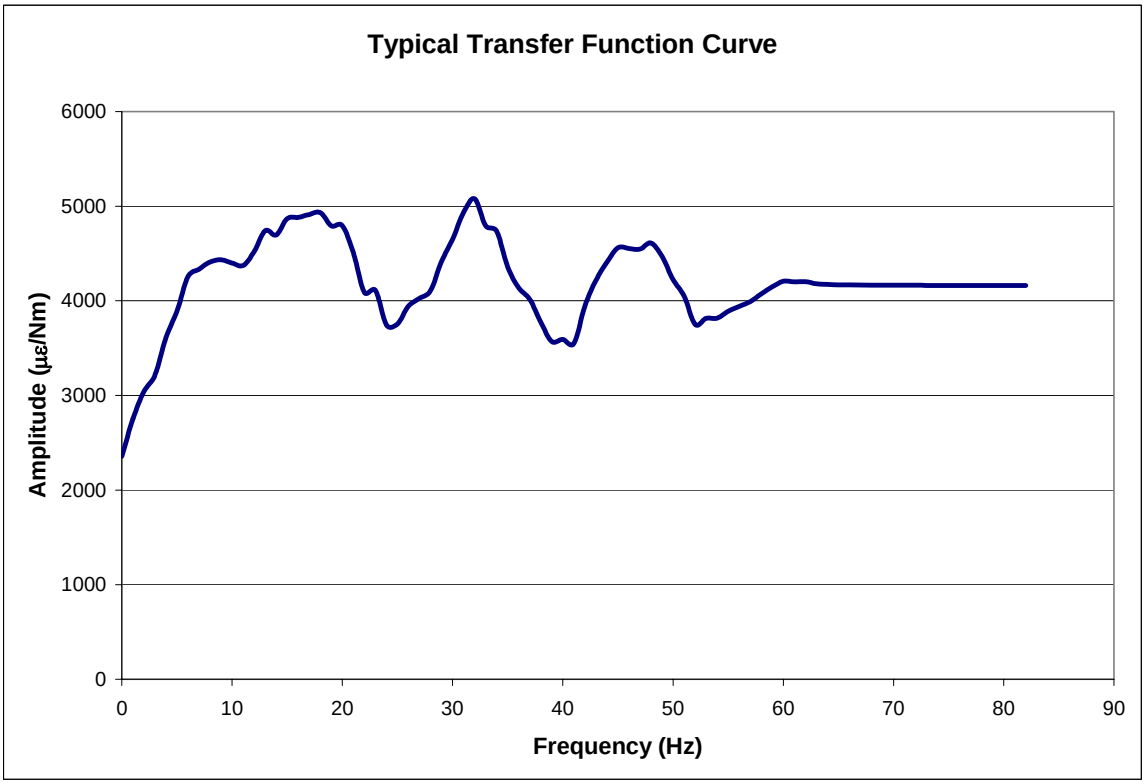

Figure 22: Typical Transfer Function Curve

Once obtained, the transfer functions were analyzed for their "high-frequency average:" and subsequently normalized by those values. The high-frequency average is equivalent to the "gain" of the system, and represents the general amplification from input to output. The resulting plots look very similar to Figure 22, so an individual plot is not repeated below. Instead, Figure 23 and Figure 24 show accumulated transfer function data for T- and P-Sync optimizations, respectively:

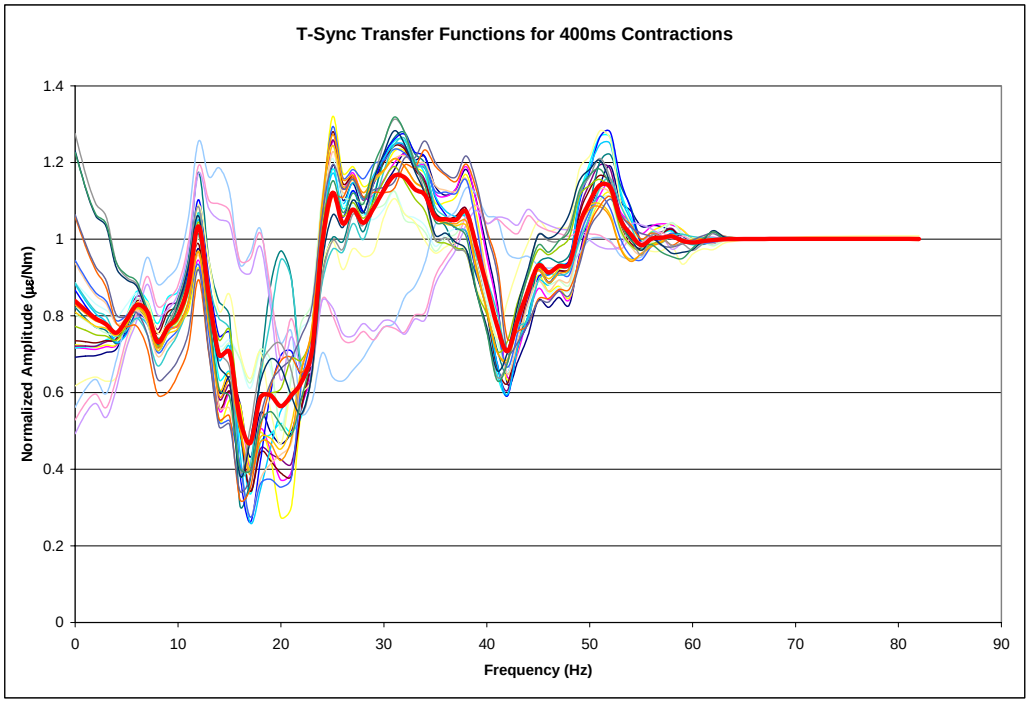

Figure 23: T-Sync Transfer Function Curves; The Dark Red Line Indicates the Average.

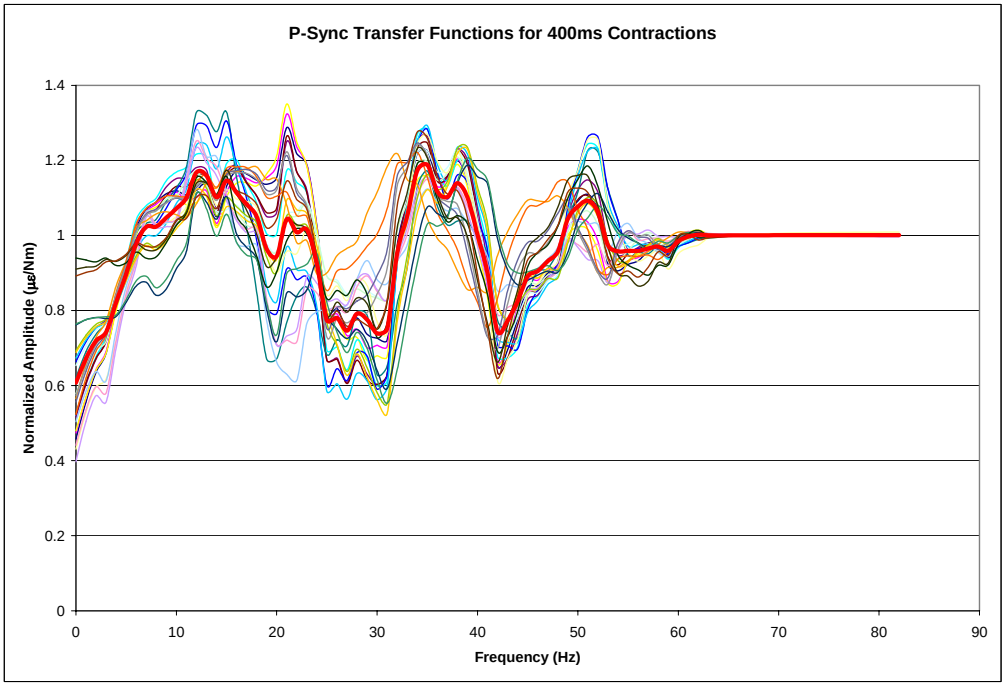

Figure 24: P-Sync Transfer Function Curves; The Dark Red Line Indicates the Average.

It is interesting to note that the above figures show transfer functions calculated from the exact same data. The only differences between them are the synchronization routine used to run the calculations. While these two figures do have some differences, they are fairly similar in overall shape. Their high-frequency components level off to a relatively flat value and they have fluctuations in the lower-frequency region. To better illustrate the differences between these transfer function calculations, Figure 25, below, illustrates the average (solid dark lines from above) curves for P- and T-Sync calculations.

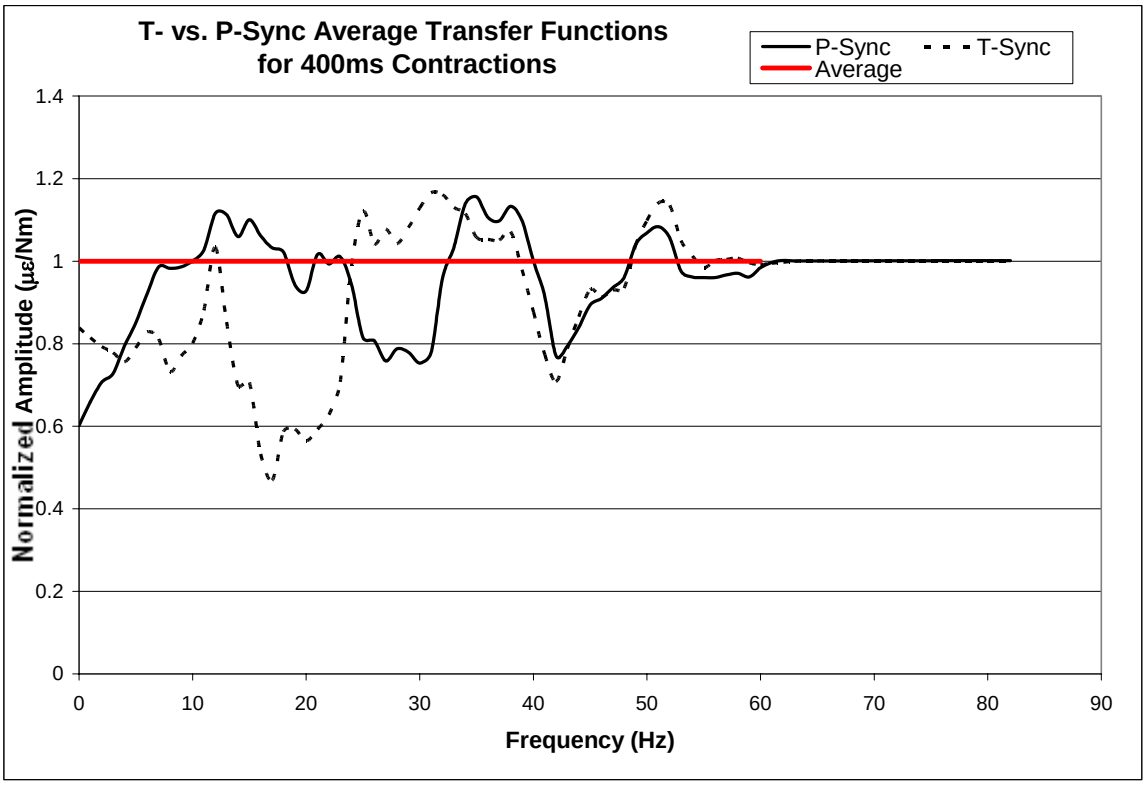

Figure 25: P- and T-Sync Average Transfer Functions for 400ms Contractions

The most interesting differences between these functions happen at the lower frequencies. Specifically, the T-Sync transfer functions show a general attenuation of 0-

25Hz signals while the P-Sync transfer functions show a less substantial attenuation in the 25-32Hz band. The calculated functions show good agreement at higher frequencies, which indicates that the gains calculated by the transfer functions are accurate. The lower-frequency variations likely appear because the P-Sync transfer function contains the extra "energy" needed to cause the signal delay. The factual accuracy of that statement may be unapparent, so I offer additional explanation. When dealing with a (relatively) low-frequency signal, the majority of the energy exists in the lower frequencies. If all frequencies need the same amount of delay to accommodate a time shift, the relative impact of a time shift will be greater where more energy exists. Since the T-sync transfer functions need minimal delay, the impact is seen most acutely in the lower bands. It makes sense that the lower frequency bands of the T-Sync transfer functions would have lower amplitudes than in the higher frequency regions. Figure 26 shows the results of taking the difference of the two curves in Figure 25, which should represent the impact of the delay on the transfer function.

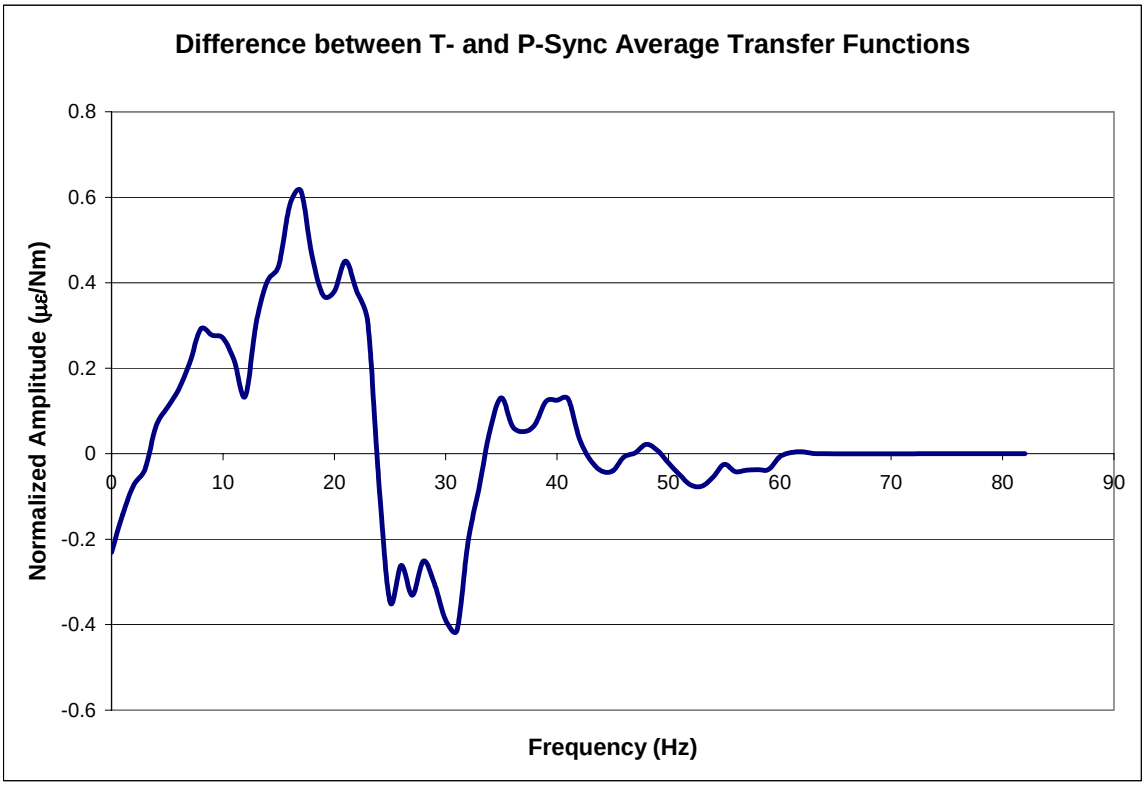

Figure 26: Difference between T- and P-Sync Average Transfer Functions

The meaning of the figure above will be explained thoroughly in the discussion. Table III shows the differences in the H-F averages (gain) of the transfer functions alongside the stiffness results obtained in Table III:

Table III. Effects of P- and T- Synchronizations on Transfer Function Gain and Linear Stiffness Calculations

	Transfer Function Gain (±S.E.)	Linear Regression Stiffness (±S.E.)
P-Sync	2300.4 ± 228.0	2378.3 ± 239.3
T-Sync	2290.8 ± 230.6	2087.0 ± 203.5

The table above shows only the averages of each group. In Table III (above), there are some striking similarities in the results calculated. Namely, the transfer function gain is nearly unfazed by delays between the signals, while the linear regression is greatly affected. The more consistent transfer function method suggests that the P-sync optimization is closer to an optimized delay than the T-sync method is. Figure 27 sheds some light on the results in Table III by plotting individual point-pairs, TF gain vs. linear regression stiffness:

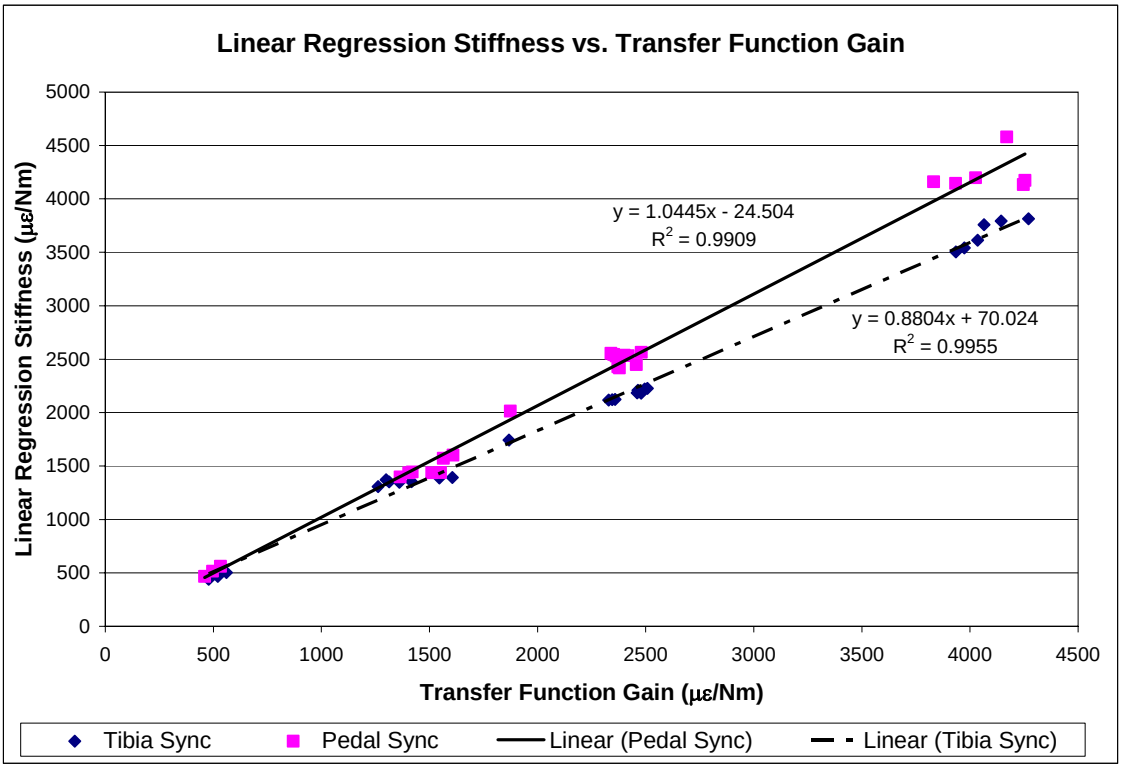

Figure 27: Linear Regression Stiffness Values vs. Transfer Function Gain Values

As you can see from the figure above, the R^2 values from the regressions are very high ($R^2 > .99$). This level of correlation affirms that the original signals are similar in shape: if the slopes of the strain and torque data were dramatically different, their linear regressions would not be cleanly linear. The fact of the regressions' good fit with transfer function gains serves to reaffirm transfer function analysis as a powerful means to explore these signals. It is also noteworthy that the pedal synchronization routine offers better 1-to-1 (slope ≈ 1) correlation between the transfer function gain and the linear regression stiffness. The lack of a perfect 1-to-1 correlation between transfer function average and linear regression stiffness leads this author to conclude that the synchronization offsets found above somehow bracket the offset value that could offer that 'perfect' correlation. To that end, the slopes of the lines in Figure 27, above, were used to interpolate (I-Sync) between the offset values found for P- and T-Sync routines. Using the found offset values from I-Sync, transfer functions and linear regressions were

calculated, and plotted as in Figure 27. Figure 28 shows those data plotted, with linear regression and R^2 value parameters identified:

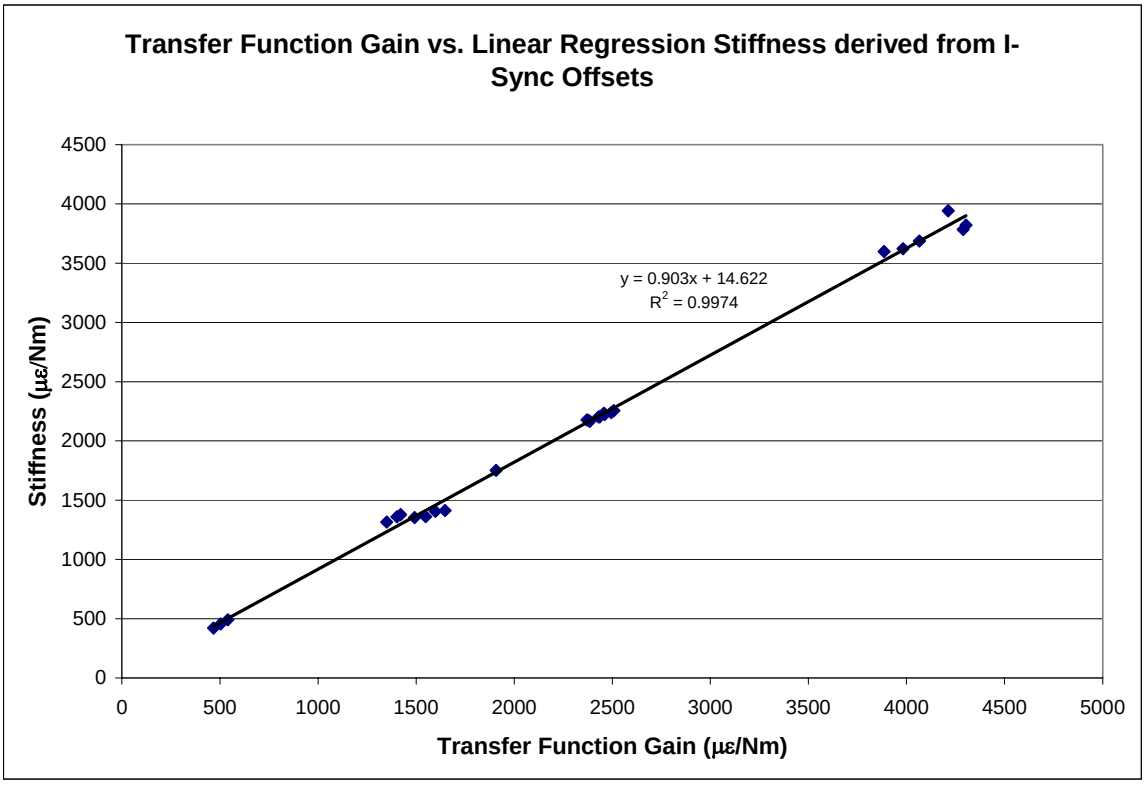

Figure 28: Transfer Function Gain vs. Linear Regression Stiffness Derived from I-Sync Offsets

As you can see in Figure 28, the slope of that linear regression is not 1. This result suggests that the effect synchronization has on the relationship between transfer functions and stiffness is non-linear. The interpolation (I-sync) method was designed to predict a synchronization offset that would allow for a 1-to-1 relationship between stiffness and transfer function gain. Since the linear interpolation model did not 'find' the 1-to-1 slope, we must conclude that the TF gain/linear stiffness relationship is not linearly dependent on offset value.

As outlined in Methods, axial gage location was recorded for each animal along with that animal's tibial length. From those measurements, we were able to express

locations of the gages both as a fraction of the tibial length and as a distance from the epiphysis. Figure 29, below, shows the results of plotting P-Sync averages vs. gage location:

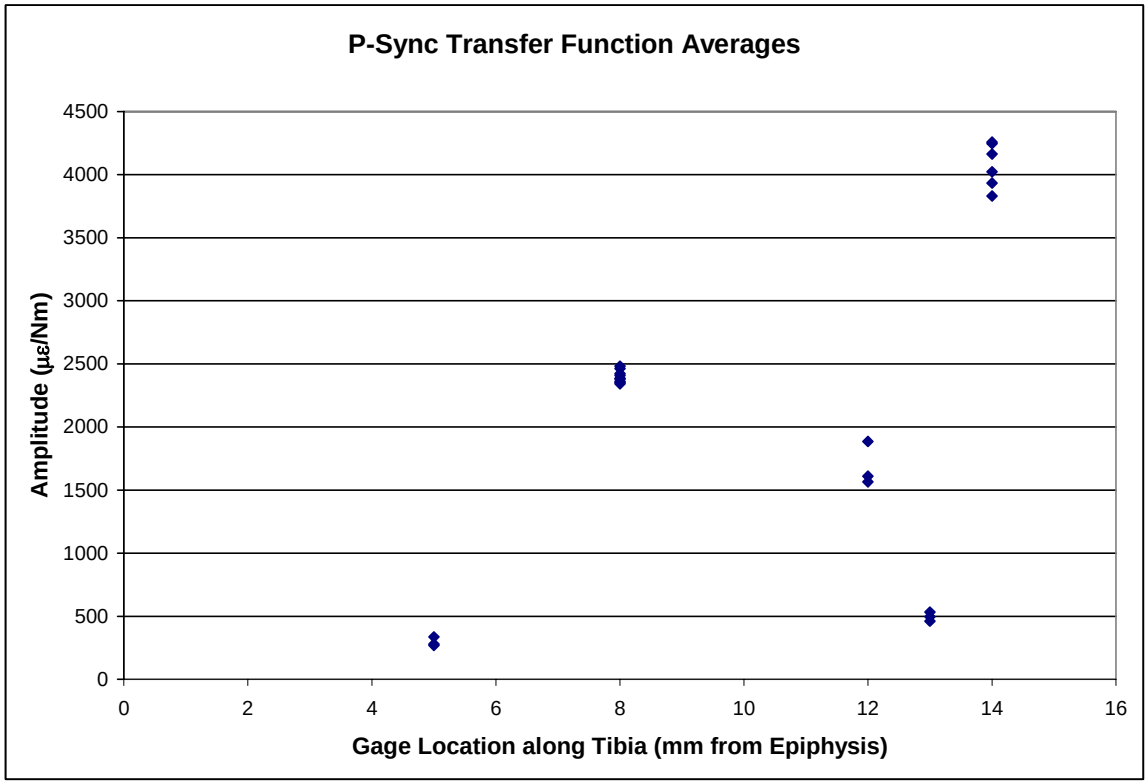

Figure 29: P-Sync Transfer Function Averages vs. Gage Location

As you can see, there is little to be had here in the way of coherent data. There seems to be a general rising trend as gage location moves away from the epiphysis, but no significances exist between those data. The possible sources of variation have been listed in the Rosette section, and will be discussed below.

After calculating the transfer functions from given data, we need a measure of how close the average of the functions comes to each individual transfer function. For this question, the coherence function was used (Eq. 17). The closer the resulting value is to one (1), the closer the fit. Figure 30 shows the results of these calculations:

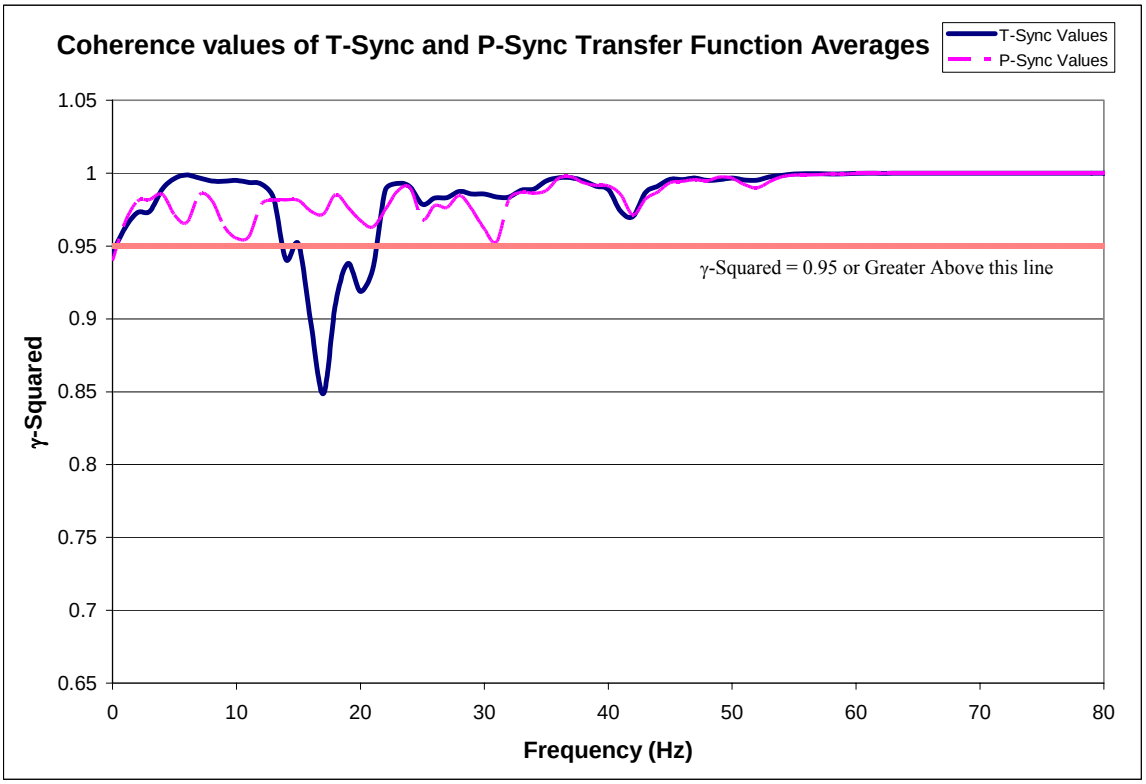

Figure 30: γ^2 Values of T- and P-Sync Transfer Function Averages

It is worth noting that the P-Sync data have much higher agreement than the T-Sync data. Overall, the averages of both transfer functions describe >85% of the total variation in the signals. Given these results, it may be possible to use these average transfer functions to predict the spectral content of strain data from torque recordings.

The final phase of this thesis investigates the potential use of these average transfer functions to predict tibial strain from torque curves. To accomplish this, the Inverse Fourier Transform (IFFT) was used to compute a time-based signal from the average transfer function illustrated in Figure 31:

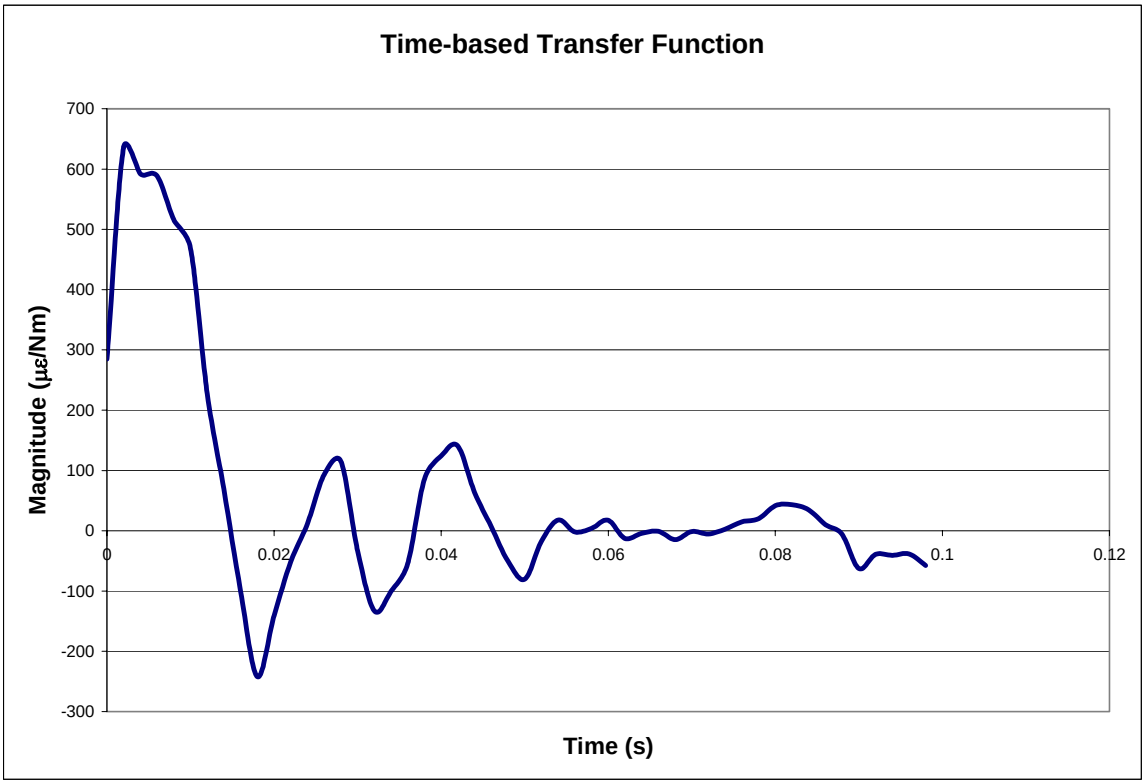

Figure 31: IFFT-Derived Time-based Transfer Function

As multiplication in the frequency domain is equivalent to convolution in the time domain, the resultant time-based signal will be convolved with the input (torque) and the results compared to the strain curve. The results of that operation on a single data set are shown in Figure 32:

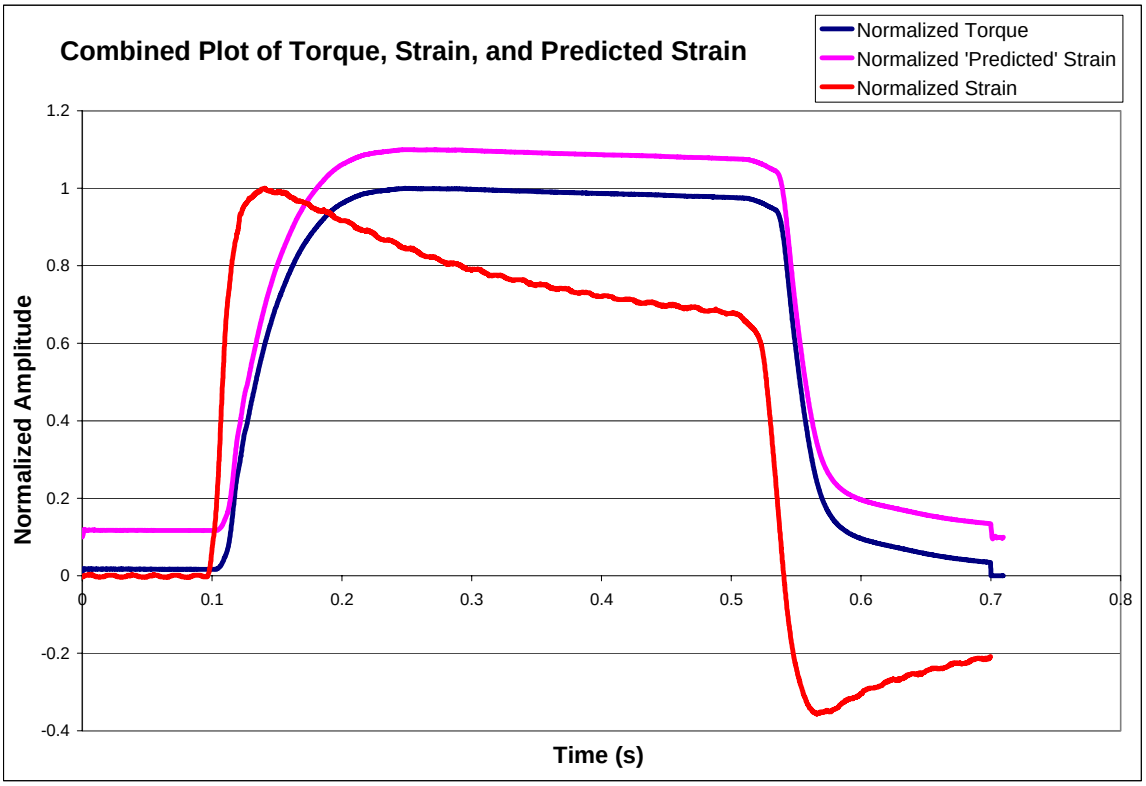

Figure 32: Combined Plots of Torque, Strain, and Predicted Strain

As you can see, the time-based signal is inadequate to properly transform the torque curve into the strain curve. A discussion on these findings can be found below.

Discussion of Transfer Function Results

To this author, the most interesting findings from the 400ms contractions are the attenuation of the lower-frequency bands in the T-Sync data. At this time, it warrants a reminder that the T-Sync routine is an area minimization between ankle torque's rising edge and tibial strain's rising edge. T-Sync is not the same routine that previous researchers used in their theses; all previous work into synchronization was done by area minimization of the entire torque curve against the strain recording. The previously used method mentioned above was used in this thesis, and can be seen in the lower left corners

of Figures 17 and 18. While these techniques only create an average of 31 samples' difference between start points (0.0062s), the stiffness values obtained from linear regression are significantly higher for the (new) T-Sync protocol.

By comparison, using any means of synchronization to find transfer functions between data yields nearly identical results for gain in the transfer function. While gain in a transfer function and linear regression stiffness are not the same thing, Figure 27 shows that the two measures of curve relation are correlated to over 99% agreement regardless of synchronization routine used. This high level of correlation suggests that transfer function gain values are sufficient replacements for synchronization-based linear regressions.

Figure 25 shows T- vs. P-Sync averages for calculated transfer functions. In that figure we see that T-Sync functions average much lower in the 0-25Hz bands than the P-Sync functions do. As mentioned above, this difference is likely a 'lead factor,' which is superimposed onto the more natural T-Sync transfer function. The result of taking this difference is found in Figure 26, and looks very similar to the difference between the Fourier transforms of two time-delayed square waves. Figure 33 shows the results of subtracting the Fourier transforms of two square waves from each other. One of the waves was delayed, and one was not:

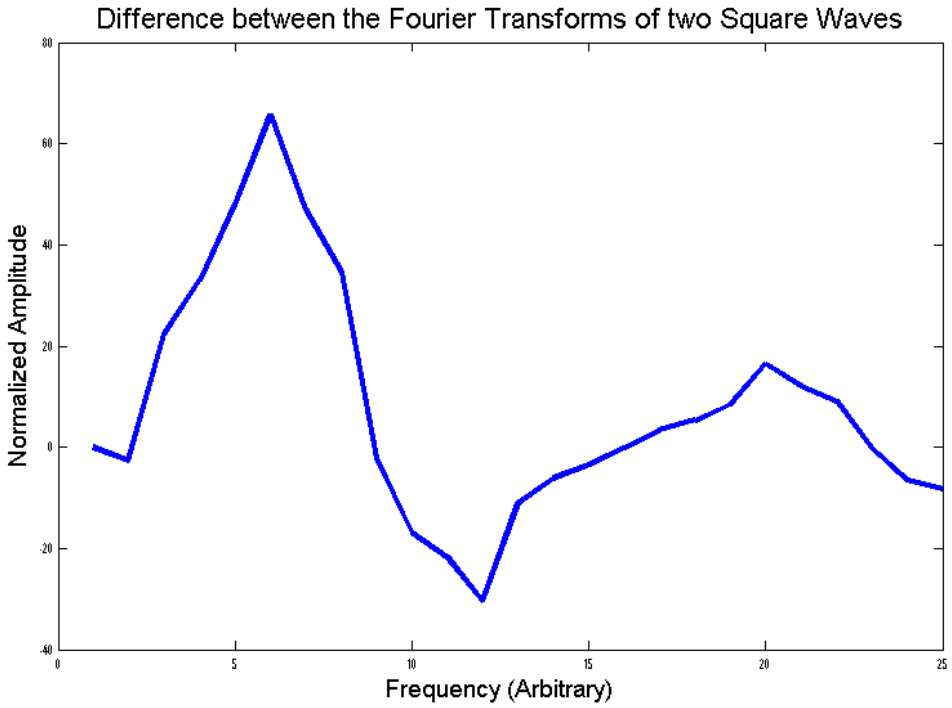

Figure 33: Exemplar Plot of Differences between Two Square Waves in Frequency Space

Note how similar Figure 26 and Figure 33 are: this similarity is fully expected given the 400ms contractions' resemblance to square wave functions. When we instituted a delay in the transfer function, we simply created the difference between the two traces in Figure 25. This finding supports the claim that the equivalence of overall transfer function gain values is invariant with temporal delay. Using transfer functions to determine relationships between signals does not fully depend on temporal delay; only the lower frequencies are affected by delay.

The γ^2 values calculated in Figure 30 demonstrate that the torque and strain data have, at least, a highly repeatable relationship. The higher degree of agreement in the P-Sync data is an interesting finding, but unexpected. There is extra energy required in causing a delay in the Fourier transform, and that extra energy serves as a unifying factor in the average. The agreement was an appealing find, but care should be taken here. The T-Sync transfer function is a much more direct calculation, and should be treated as such.

If one wanted to calculate gain values, any synchronization method would be acceptable, but for linear regression, synchronization is crucial in interpreting the results.

The final operation presented above was the convolution of the transfer function IFFT with the input signal. The results of that operation were presented in Figure 32, and show little success in predicting strain values from transfer function averages. There are several problems interfering with the success of this approach: of them, features of Eq. 15 and truncation errors in the transfer function are the most problematic.

In Eq. 15, we see that the direct relationship between two signals is due to the square of the magnitude of the transfer function. This relationship necessarily destroys phase information about the transfer function, leading to a transfer function whose magnitude is correct, but whose phase information is lost. Reproducing a curve from magnitude sans-phase cannot be properly done. The direct IFFT of a transfer function calculated from Eq. 15 cannot produce the time-based signal as desired.

Fortunately, the transfer functions are derived from spectral inputs and are valid for spectral relationship inferences. Specifically, the transfer functions show that attenuation between torque and strain occurs in the 24-32Hz band. This may be physiological in origin: nerve impulses to muscle occur at roughly 30Hz. The attenuation, or "soft tissue effects" at those frequencies would serve to calm the impulses into smooth motion.

Truncating the transfer function eliminates some of the energy originally calculated between the signals. After truncation, performing an IFFT results in an incomplete time-based signal. Without a doubt, there exists a time-based signal to relate torque and strain waveforms via convolution. Unfortunately, the approach cited in this thesis is inadequate to derive that waveform.

CONCLUSIONS AND RECOMMENDATIONS

From the combined plots of Figure 18 and Appendix C, it appears that using the toes of the torque and strain curves as synchronization defaults would increase the repeatability and accuracy of torque-strain synchronization. When we compare the results from synchronized linear regressions to those from transfer functions, it becomes clear that synchronizing pedal strain to ankle torque (P-Sync) may provide a better linear regression stiffness value than the synchronization of tibial strain to ankle torque (T-Sync). Either synchronization method effectively predicts overall gain with transfer functions, meaning the additional complication arising with recording pedal strain is unnecessary if using transfer functions. Future work will need to keep in mind that the values found in either transfer function shapes or linear regression stiffness are dependent on synchronization, and use the methods that work best for the intended analysis. Some results, like transfer function high-frequency gain, however, do not vary with synchronization routine.

It appears that transfer function gain accurately represents the linear regression stiffness values calculated earlier in this work. Previous work and data collected by other researchers has been investigated by the author, but differences in the method and type of muscle stimulations make their strain gage recordings unavailable for use.

At this point, a renewed discussion is merited on the actual meaning of the computed transfer function. There are unavoidable biases in the recording computers for both strain and torque, which can have an effect on the shapes of the transfer functions. More to the point, it is unwise to assume from these data that the shapes of these transfer functions are solely dependent on the reactions of the rodent leg. The calculated transfer functions represent the frequency response of the entire system, which includes the rat leg, and both measurement systems. While the effects of the mechanical systems were not investigated here, this author believes that the overall effect is minimal. Since strain predictions are sought from torque waveforms and the recorded torque data already have the bias incorporated, the transfer functions automatically correct the biases to accurately predict the relationship between recordable torque and recordable strain.

The majority of this thesis has focused on 400ms contractions for mathematical analysis, despite there never having been a 400ms contraction used in previous work by our lab. The reasons for this contraction length were originally to provide separable regions in the strain profile for analysis. Specifically, loading, holding, and unloading regions of each curve were to be evaluated against a generalized linear model for viscoelasticity. This model was intended to provide an effective means of predicting strain based on torque production. In order to properly calculate the relationship, we need a causal relationship to exist where our measurable parameter (torque) causes an immeasurable parameter (strain). When it was determined that strain in the tibia leads (occurs before) torque production at the ankle, viscoelastic models had to be thrown out because no physical system can cause an output that is dependent on future values of input (non-causal). The search for a physical analog model of the ankle had to be abandoned temporarily due to time and scope constraints on this work. A spring-mass-damper transfer function may be eventually found that will accurately represent the shape changes between torque and strain waveforms, but much more work is required before accurate predictions of parameters can be accomplished. Future work in this field may focus on the muscle stimulation signal (square wave of electrical current) as the true 'input' of the system and evaluate that input versus the dual outputs of ankle torque and tibial strain. This method of analysis is outside the scope of this thesis and is not shown here. Other work in this vein may experiment with introducing false lag into the strain data, or experimenting with a more advanced single input, multiple output system (SIMO).

Introducing artificial lag into the torque-strain system is an accepted method of introducing causality into an otherwise non-causal system. A small tradeoff of that method would be that the strain traces acquired would not be temporally relevant to torque; in other words, only the shape of the strain curve would be obtainable. I doubt that this tradeoff would be a substantial burden on research, as knowledge of the strain environment would still be obtainable without surgery. This method may be the most promising way to relate torque to strain, but will require more research.

A SIMO system is more mathematically difficult to calculate, but would allow the simultaneous relation of stimulation waveforms (electrical shock pattern) to both torque

and strain outputs. From those data, calculating strain environments would only require knowledge of the electrical stimulation waveform.

One of the major disappointments in pursuing this thesis has been the rosette gage results. I expected this section of analysis to be much more detailed and nuanced; instead, I found no results. If the assumptions mentioned above are correct, I believe it would take approximately 100 animals to correctly identify the surface strain characteristic of the stimulated rat tibia. The methods would be very refined, and multiple animals used at each data point. This would be an unfeasibly large study that cannot promise irrefutable results.

Another comment I'd like to make is one on the possibility of repeating strain gage surgeries. In the original AUP, a sterile surgery was called for to implant a 1st strain gage, with a secondary gage implantation surgery to follow after the rat had healed. This design was meant to maximize the number of readings I could acquire off my allotted number of animals. Upon opening the strain gage site during the second surgery, it was noted that the original gage location was clearly obstructed by bony growth at the gage site, even after 3 weeks' healing time. My next attempt on a new animal was 5 weeks after the first operation, with identical results. Since the gage location targeted for attachment had already been used, a new site had to be found. Strain recordings from those two second surgeries were taken, but their results were not reliable, and were not included in this thesis.

Applying a strain gage to the muscle stimulation machine was a first for our lab; the synchronization power that strain gage gave us yielded valuable insight into the nature of ankle torque and strain interactions in the rat leg. I had assumed that temporal synchronization of torque and tibial strain would allow a greater level of calibration, but no predictive measures have come out of this work to date. Theoretically, taking the inverse Fourier transform (IFFT) of a transfer function could yield a time-based signal that can span the shape gap between torque and strain. In reality, the differences in gains between different animals and the physical impossibility of the system (non-causality), where the expected output occurs before the defined input, makes obtaining that time-based signal very difficult.

This thesis was successful in identifying a more direct means of calculating the gains between torque and strain signals, but the specifics of shape changes between those signals have yet to be fully quantified. Overall, the transfer functions derived above show a marked improvement in our understanding of the dynamics of muscle contraction-induced deformation of the rat tibia. Frequencies lower than 32Hz are typically attenuated by the leg, possibly an artifact of muscular contraction and soft tissue interactions with bone.

A final word about previous research; the Lamothe paper referenced above[11] used Fourier transforms to investigate frequency responses to bone growth in the leg, but those researchers overlooked a particularly sticky point in frequency analysis. The act of inserting spaces in a signal does not change the nature of the signal, but rather the time periods over which it acts. A 30Hz sine wave is a 30Hz sine wave, regardless of how long it lasts. The conclusion that the increased power in low frequencies, even if accompanied by higher-frequency waveforms, directly caused additional bony growth is incomplete. A more direct means of interpreting those data would be to consider the rate of cellular activation as a function of frequency along with the time period required for cellular action[9]. The proper combination of rapid cellular activation with sufficient rest time to allow those cells to function is the true goal of this and other exercise studies. While this study cannot purport to have solved the question of optimized exercise single-handedly, the frequency-response data presented here can prove valuable to future researchers looking to maximize bony response to simulated exercise.

REFERENCES

1. Currey JD. Bones: structure and mechanics. Princeton: Princeton University Press; 2006

2. Jeffrey JM. Quantifying the strain response in the rat tibia during simulated resistance training used as a disuse countermeasure. MS Thesis. Texas A&M University. 2007

3. Vyvial BA. Characterizing strain in the proximal tibia during electrical muscle stimulation. MS Thesis. Texas A&M University. 2006

4. Pisani TJ. Essentials of strength of materials. New York: D. Van Norstrand Company; 1964

5. Beer FP, Johnston ER, DeWolf JT. Mechanics of materials. New York: McGraw-Hill; 2002

6. Goodship AE, Lanyon LE, and McFie H. Functional adaptation of bone to increased stress: an experimental study. J Bone Joint Surg Am. 1979;61A:4-539

7. Qin YX, Rubin CT, and McLeod, KJ. Nonlinear dependence on loading intensity and cycle number in the maintenance of bone mass and morphology. J Orthop Res. 1989;16:482

8. Rubin CT, and Lanyon LE. Regulation of bone mass by mechanical strain magnitude. Calcf Tiss Intl. 1985;37:411

9. Bacabac RG, Smit TH, Mullender MG, VanLoon JJWA, Klein-Nulend J. Initial stress kick is required for fluid shear stress-induced rate dependent activation of bone cells. Annls Biomed Engr. 2005;33:1-104

10. Bacabac RG, Smit TH, Mullender MG, Dijcks SJ, VanLoon JJWA, et al. Nitric oxide production by bone cells is fluid shear stress rate dependent. Biophys Res Comm. 2004;315:4-823

11. LaMothe JM, Zernicke RF. Rest Insertion combined with high-frequency loading enhances osteogenesis. J App Phys. 2004;96:1788

12. Srinivasan S, Ausk BJ, Poliachik SL, Warner SE, Gross, TS, et al. Rest-inserted loading rapidly amplifies the response of bone to small increases in strain and load cycles. J App Phys. 2007;102:1945

13. Alcorn TD. Osteogenic effect of electrical muscle stimulation as a countermeasure during hindlimb unloading. MS Thesis. Texas A&M University. 2006

14. Cromwell L, Weibell FJ, Pfeiffer EA, Usselman LB. Biomedical instrumentation and measurements. Upper Saddle River: Prentice Hall; 1973

15. Lessard CS. Signal processing of random physiological signals. San Rafael: Morgan and Claypool; 2003

16. Dym, H and McKean, HP. Fourier series and integrals. Prob Math Stud. New York: Academic Press; 1972;14

17. Cochran WT, Cooley JW, Favin DL, Helms HD, Welch PD, et al. What is the fast fourier transform??. IEEE Trans Audio Electr. 1967;AU-15:2-45

18. Bergland GD. A guided tour of the fast fourier transform. IEEE Spectrum. 1969;6:7-41

19. Lawrence RR, McClellan JH, and Parks, TW. FIR digital filter design techniques using weighted chebyshev approximation. Proc IEEE. 1975;63:4-595

20. Schmit, J and Creath, K. Window function influence on phase error in phase-shifting algorithms. Appl Optics. 1996;35:28-5642

21. Cordaro NM, Weiss JA, and Szivek, JA. Strain transfer between a CPC coated strain gauge and cortical bone during bending. J Biomed Matls Res. 2001;58:2-147

22. Levine DM, Ramsey PP, and Smidt RK. Applied statistics for engineers and scientists. Upper Saddle River: Prentice Hall; 2001

23. Gray, H. Pick, P., and Howden, R. Gray's anatomy. Philadelphia; Lea&Febiger; 1918

APPENDIX A
PROGRAM FLOWCHARTS FOR DATA ANALYSIS

Torque/Strain Peak Value Calulator Flowchart

Process chart for calculating peak to peak gains between torque and strain

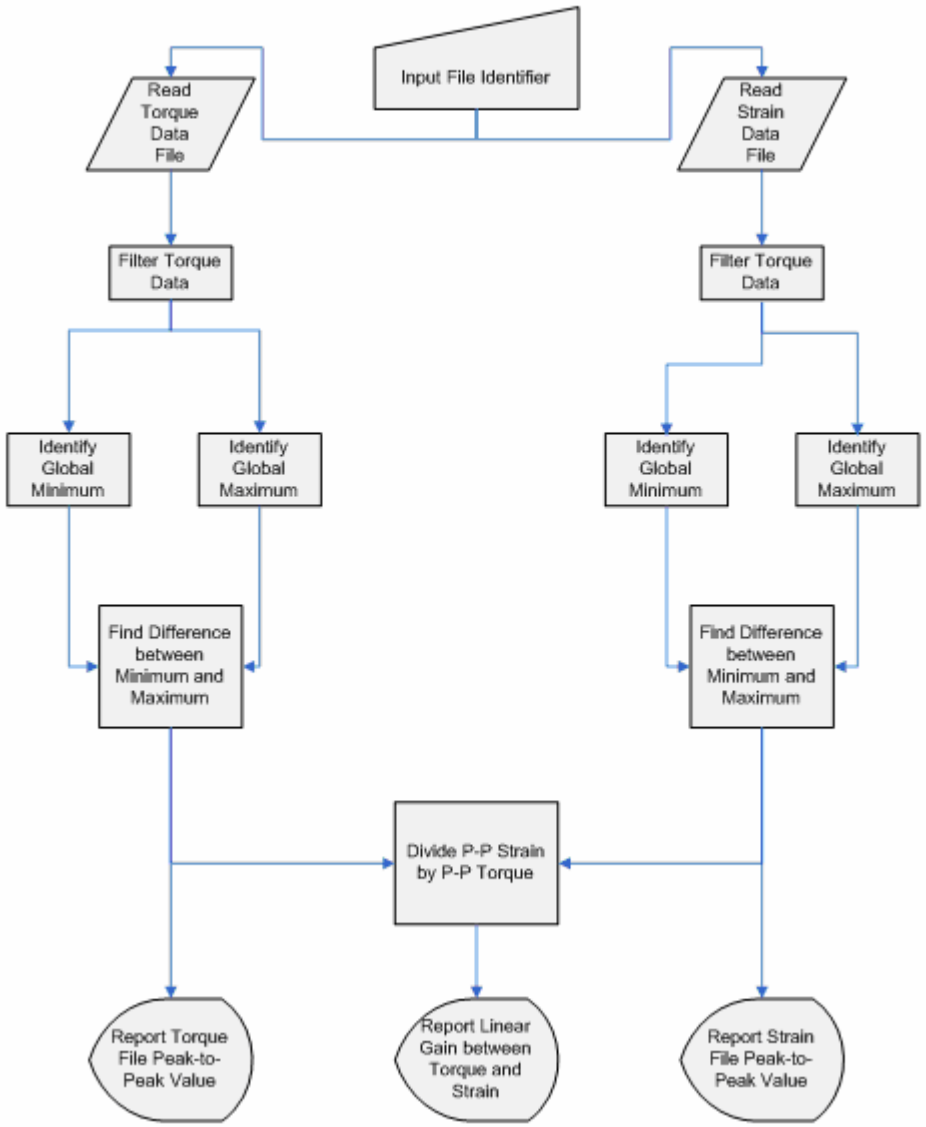

Principal strain calculation Flowchart

Process chart for calculating principal strains from raw rosette recordings

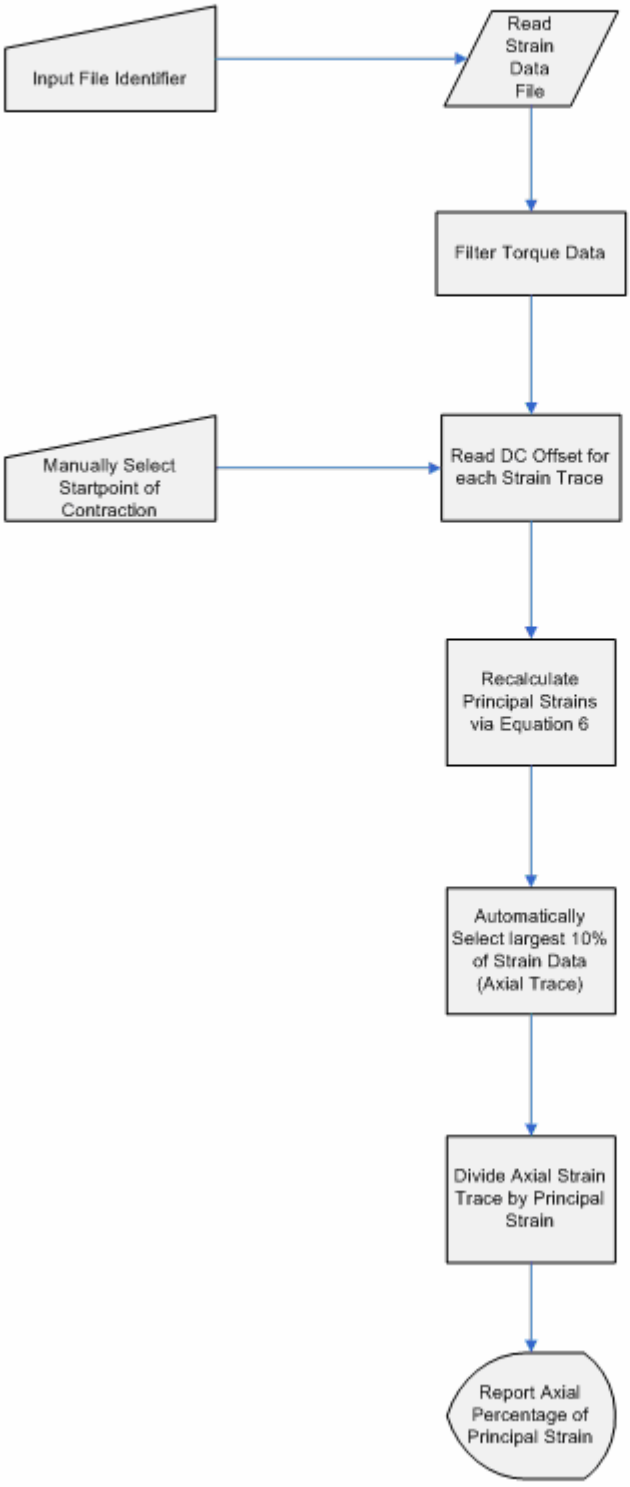

Torque/Strain Synchronization Flowchart
Universal process chart for integration based synchronization

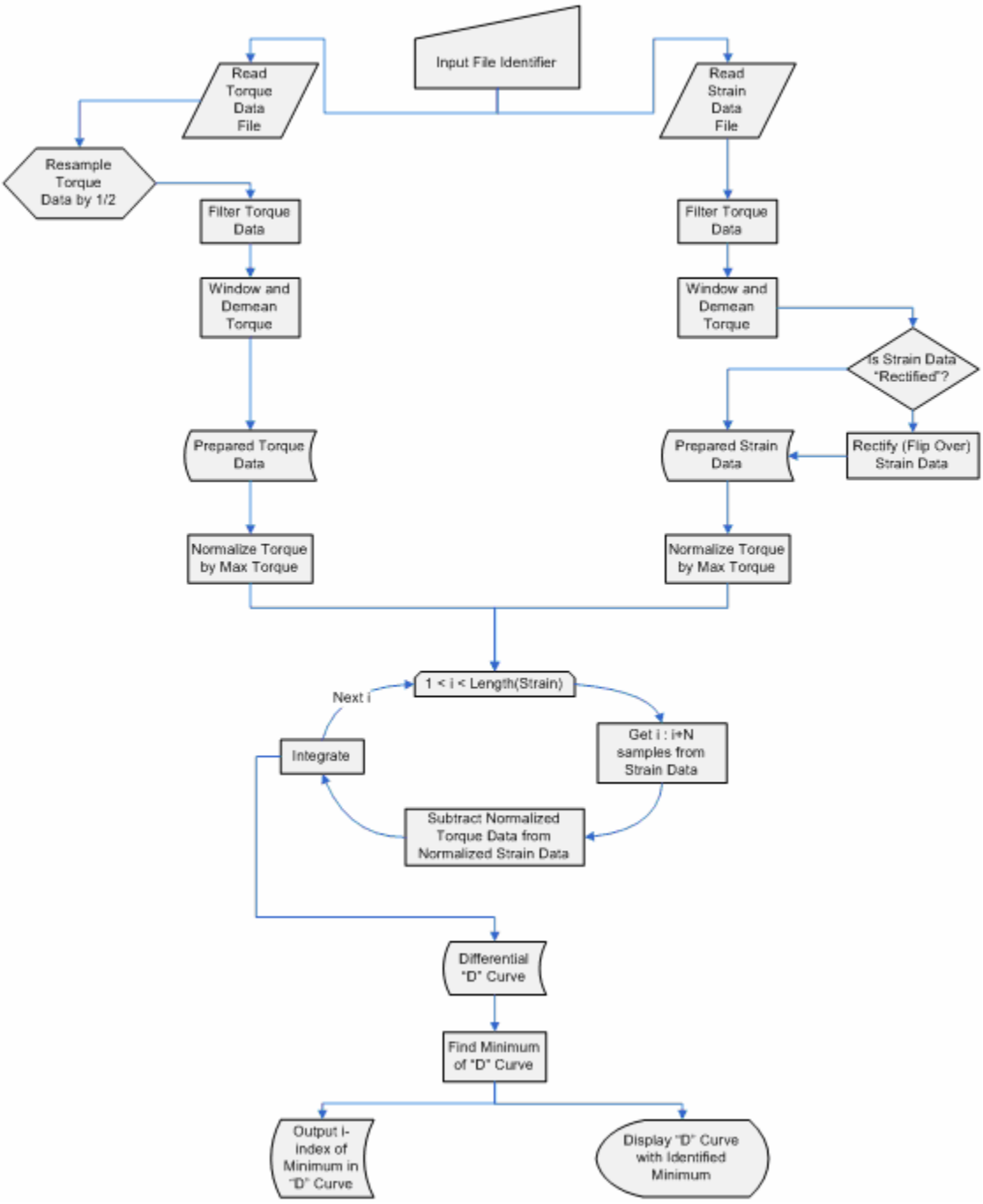

DADiSP Transfer Function Computation Flowchart

Process chart for transfer function calculation

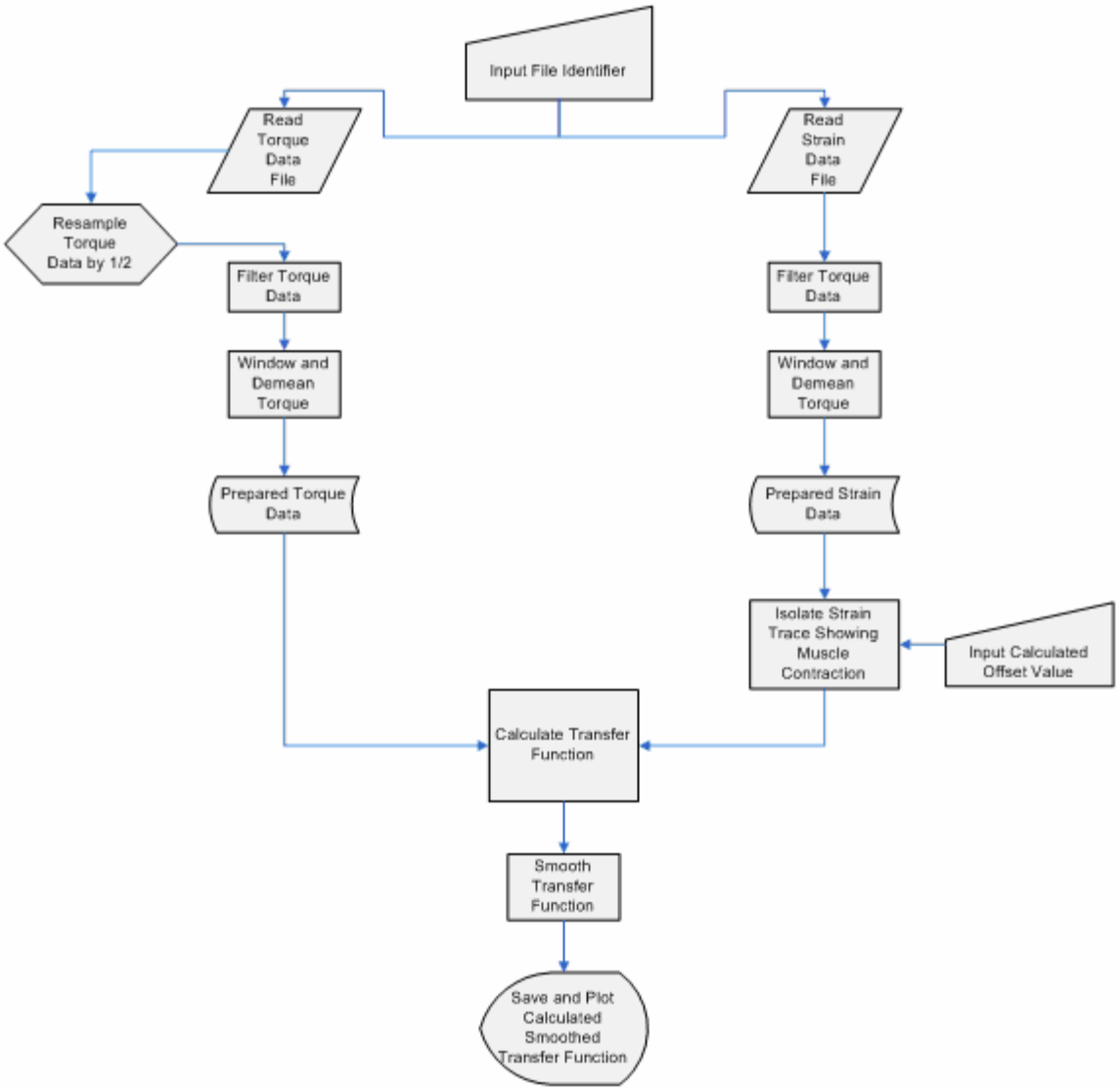

APPENDIX B
STATISTICAL RESULTS

Paired t-test: Thursday, July 17, 2008, 12:56:42 PM

Data source: Linear Regression data in Thesis Data.SNB

Normality Test: Passed (P = 0.165)

Treatment Name	N	Missing	Mean	Std Dev	SEM
PedToeStiffness	26	0	2378.312	1220.119	239.285
TibToeStiffness	26	0	2086.983	1037.484	203.467
Difference	26	0	291.329	203.633	39.936

t = 7.295 with 25 degrees of freedom. (P = <0.001)

95 percent confidence interval for difference of means: 209.080 to 373.578

The change that occurred with the treatment is greater than would be expected by chance; there is a statistically significant change (P = <0.001)

Power of performed test with alpha = 0.050: 1.000

Linear Regression Wednesday, July 16, 2008, 2:39:34 PM

Data source: Linear Regression data in Thesis Data.SNB

Stiffness = 453.525 + (7179.200 * Gage Placement)

N = 58 Missing Observations = 6

R = 0.247 Rsqr = 0.0612 Adj Rsqr = 0.0444

Standard Error of Estimate = 1376.536

	Coefficient	Std. Error	t	P
Constant	453.525	1008.630	0.450	0.655
Gage Placement	7179.200	3758.472	1.910	0.061

Analysis of Variance:

	DF	SS	MS	F	P
Regression	1	6913601.344	6913601.344	3.649	0.061
Residual	56	106111617.332	1894850.309		
Total	57	113025218.675	1982898.573		

Normality Test: Failed (P = 0.018)

Constant Variance Test: Failed (P = 0.009)

Power of performed test with alpha = 0.050: 0.465

The power of the performed test (0.465) is below the desired power of 0.800.
Less than desired power indicates you are less likely to detect a difference when one actually exists.
Negative results should be interpreted cautiously.

VITA

Author:
Scott Daniel Bouse

Degrees:
Bachelor of Science in Biomedical Engineering, Texas A&M University, May 2006

Address:
Department of Mechanical Engineering
Attn: Harry Hogan
3123 TAMU
College Station, TX 77843